

Geochemical characteristics of igneous host rocks of Lubin-Zardeh Au-Cu deposit, NW Iran

H. Zamanian^a, S. Rahmani^{a,*}, R. Zareisahamieh^a, A. Pazoki^a, X.Y. Yang^b

^a Department of Geology, Faculty of Sciences, Lorestan University, Khorram Abad, Iran

^b School of Earth and Space University of Science and Technology of China, China

ARTICLE INFO

Keywords:

Lead
Strontium-neodymium isotope
Trace element and REE
Quartz monzonite
Lubin-Zardeh
West Alborz

ABSTRACT

The Lubin-Zardeh Au-Cu ± Pb ± Zn deposit is located in the Azerbaijan-Western Alborz zone, 45 km NE of Zanjan, Iran. It is situated within the Eocene-Oligocene volcanic-plutonic belt of the Tarom subzone of the Alborz mountains range. Quartz monzonite and tuffs are the main host rock of the Lubin-Zardeh Au-Cu ± Pb ± Zn deposit. Granitoid rocks are predominantly high-K, calc-alkaline with shoshonitic affinities. They are I-type, metaluminous, magnesian and are characterized by LILE, LREE and Th enrichment relative to HFSE, depletion in Nb, Ta, Ti and weak depletion in HREE and Y. These granitoids show some affinities with adakites, e.g., high Sr/Y and La/Yb ratios coupled with low Yb and Y, and enrichment in LREE and LILE with weak Eu anomalies. Their relatively low to moderate initial $^{87}\text{Sr}/^{86}\text{Sr}$ values (0.7047–0.7051), positive Nd ($t = 36$ Ma) values (0.39–2.1) and TDM ages of 0.69 to 1.06 Ga, with Pb isotopic ratios of initial $^{206}\text{Pb}/^{204}\text{Pb} = 18.49\text{--}18.68$, initial $^{207}\text{Pb}/^{204}\text{Pb} = 15.58\text{--}15.61$ and initial $^{208}\text{Pb}/^{204}\text{Pb} = 38.33\text{--}38.77$, are consistent with a phlogopite-bearing, amphibole-rich, and enriched lithospheric mantle source metasomatized by earlier subducted sediments. The geochemical and isotopic compositions of the granitoids are similar to the host rocks of porphyry and epithermal deposits in the Urumieh-Dokhtar zone.

1. Introduction

Subduction of Neo-Tethys oceanic crust beneath the Iranian plate, and subsequent collision of the Arabian platform with Eurasia during the Alpine-Himalayan orogeny caused the formation of the orogenic Sanandaj-Sirjan Zone (SSZ), the Urumieh-Dokhtar Magmatic Arc (UDMA), the Alborz Magmatic Belt (AMB) and the Zagros Fold and Thrust Belt (ZFTB; Nabatian et al., 2016). The SSZ is considered as the main magmatic arc resulting from Neo-Tethyan subduction during the Mesozoic (Azizi et al., 2011; Berberian and King, 1981), whereas the UDMA and AMB are interpreted to be associated with early to late Cenozoic subduction-related magmatism on the Zagros hinterland (Berberian and King, 1981; Berberian et al., 1982; Stöcklin, 1971, 1968), slab break-off (Agard et al., 2011; Ghasemi and Talbot, 2006; Haschke et al., 2010), slab roll-back (Jahangiri, 2007; Verdel et al., 2011) and post-collisional relaxation (Castro et al., 2013; Nabatian et al., 2014). The tectonic evolution of the Neo-Tethys Ocean in Iran is associated with different ore deposits types, most of which are porphyry copper and epithermal gold deposits (Yang et al., 2009).

The AMB is situated in northern Iran, which includes the Tarom Magmatic Belt (TMB) in the west and the UDMA, Tertiary magmatic

belt, that runs parallel to the main NW-trending ZFTB (Azizi and Moinevaziri, 2009; Azizi and Jahangiri, 2008; Fig. 1).

In view of metallogenetic characteristics, the western Alborz-Azerbaijan Zone includes Tarom and Ahar-Arasbaran metallogenetic belts (Aghazadeh et al., 2011, 2013; Nabatian et al., 2016).

In the TMB, plutonic (quartz monzonite) and volcaniclastic rocks (tuff) host Cu-Au ± Pb ± Zn and Mo mineralization and the Lubin-Zardeh is one of the mineral deposits. Various styles of mineralization, such as dissemination and veinlets, stockwork veins and vein breccias can be observed. The host rocks of these deposits exhibit strong hydrothermal alteration, including sericitic, argillic and silicic alteration types. The Lubin-Zardeh Au-Cu ± Pb ± Zn deposit, a small-sized (0.5 Mt averaging 1.3% Cu, 0.7% Pb, 0.4% Zn, 0.52 ppm Au) deposit (Rahmani, 2010; Zamanian et al., 2016), is located in the TMB, approximately 45 km northeast of the city of Zanjan, northwestern Iran (Fig. 1).

Based on the overall geological setting, alteration patterns and geochemical features, the Lubin-Zardeh Au-Cu ± Pb ± Zn deposit is considered an epithermal Au-Cu deposit (Zamanian et al., 2019). It is generally believed that epithermal Au-Cu ± Pb ± Zn mineralization in the TMB is related to the emplacement of Oligocene granitoids that

* Corresponding author.

E-mail address: rahmanishahram581@yahoo.com (S. Rahmani).

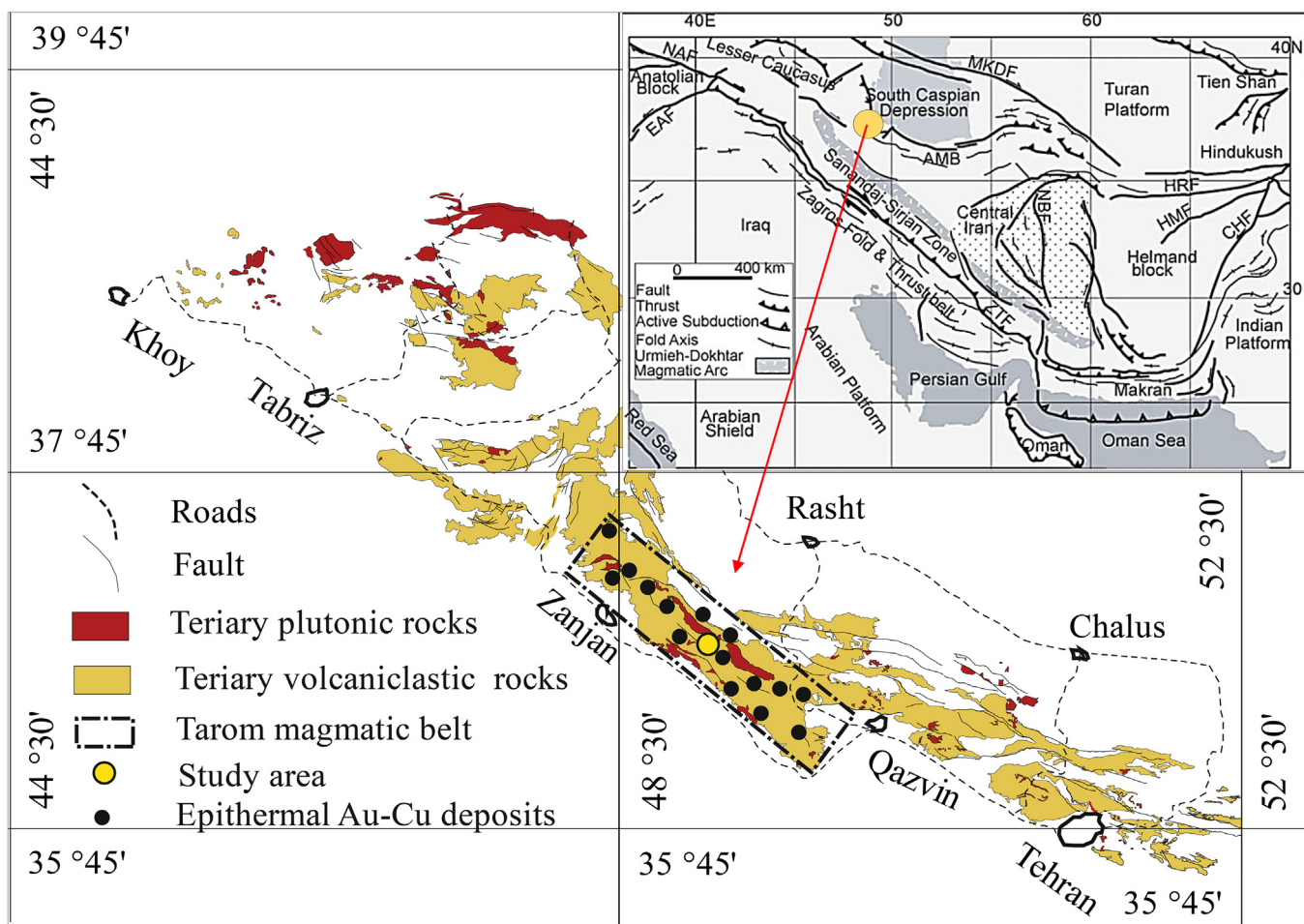


Fig. 1. Simplified structural map of Iran. Inset shows the location of the western AMB. Geology schematic map showing Cenozoic plutonic and volcanics rocks of NW Iran. Rectangle shows the location of TMB. Yellow solid circle shows the location of study area. (For interpretation of the references to color in this figure legend, the reader is referred to the web version of this article.)

have been intruded voluminous Eocene volcanic and volcaniclastic rocks (Aghazadeh et al., 2011, 2013; Kouhestani et al., 2019; Mehrabi et al., 2016; Nabatian et al., 2016; Zamaniān et al., 2019).

The Lubin-Zardeh intrusive complex exhibits geochemical features similar to adakites. Adakitic provinces have been identified in the NW of Iran (Jahangiri, 2007; Jamali and Mehrabi, 2015), in the central part of the Zagros orogen, around Anar (Omranī et al., 2008), in the eastern Iran, Bibi-Maryam (Delavari et al., 2014), and in the southeastern part of the UDMA that is considered to be one of the main Au-Cu-bearing regions in the world and studied by many authors (e.g., Asadi et al., 2014; Ayati et al., 2013; Richards et al., 2012; Shafiei et al., 2009; Zarasvandi et al., 2007, 2005, 2015, and others). It is thought that ore-hosting porphyry systems of UDMA are generally restricted to Miocene intrusions (e.g., Shafiei et al., 2009) and shown that they have an adakitic affinity (Asadi et al., 2014; Richards et al., 2012; Shafiei et al., 2009; Zarasvandi et al., 2015). It has also been recognized that geochemical adakitic signatures are often associated with Cu-Au mineralization, such as porphyry copper deposits and epithermal gold systems (e.g., Defant et al., 2002; Oyarzun et al., 2001; Qu et al., 2004; Thieblemont et al., 1997; Zhang et al., 2001, 2002).

In previous studies in the TMB and in the present study, it has been postulated that a highly metasomatized mantle source with an increasing role of amphibole and garnet (0–10%) in the genesis of the relatively younger granites (Aghazadeh et al., 2011, 2013; Nabatian et al., 2016) and geochemical characteristics indicate that the multi-phase Lubin-Zardeh intrusive complex has many adakitic petrogeochemical characteristics, but is geodynamically poorly constrained. A

detailed account of the petrology and geochemistry of this prominent intrusive complex is presented here that addresses its petrogenesis, of which the results help to a better understanding the complex magmatic evolution in an active continental margin setting during subduction and possibly collision.

2. Geology

2.1. Regional geology

The geology of Iran has been significantly affected by the opening and closure of the Neo-Tethyan oceanic branches (Aghazadeh et al., 2011, 2013; Azizi et al., 2011; Berberian and King, 1981; Nabatian et al., 2016). The subduction process and closing of Neo-Tethys caused concomitant magmatism and collision followed by the formation of Urumiyeh-Dokhtar and AMB, especially in the Sanandaj-Sirjan area (Fig. 1). The AMB is located in northern Iran, extending for about 2000 km from the lesser Caucasus in Armenia and Azerbaijan at the northwest to the Paropamisus mountain of northern Afghanistan at the east. The AMB is part of the largest mountain belt of the Alpine-Himalaya belt and is located between the Caspian Sea to the north and the Iranian Plateau to the south. The range has many summits such as Damavand in the center and Sahand and Sabalan in the western part of the belt (Azizi and Moinevaziri, 2009). AMB magmatism began in the Eocene with the development of volcanic rocks and continued in the Oligo-Miocene with emplacement of intrusive bodies. In the TMB, the Eocene deposits include abundant lava flows and pyroclastic deposits.

Eocene volcanism in the TMB started with mafic rocks composition followed by mafic-intermediate and finally felsic rocks. These rocks mainly include trachyandesite, dacite and rhyolite. Pyroclastic rocks are dominantly of felsic and intermediate composition. Several large and small plutons form the Arasbaran-Tarom batholith in the western and central part of AMB cut the Eocene rocks and are covered by the Miocene red beds (e.g., Aghazadeh et al., 2011, 2013).

2.2. Local geology

The Lubin-Zardeh area is situated to the northeast of Zanjan, TMB and comprises a sequence of Eocene and Oligocene volcanic and volcanoclastic rocks, intruded by Oligocene plutonic rocks (Fig. 1). The Lubin-Zardeh deposit consists of nine gold and base metal-bearing veins that occupy strike-slip and normal faults (Zamanian et al., 2019). The veins display similar geometrical and textural characteristics, and have regular sharp contact with volcanoclastic and intrusive rocks. Two major lithological units are recognized in the Lubin-Zardeh deposit district: (1) Eocene volcanic and volcanoclastic rocks; (2) Oligocene intrusive rocks (Aghazadeh et al., 2013; Nabatian et al., 2016). The volcanoclastic rocks include crystal tuffs and tuffaceous sandstones (Hirayama et al., 1966). The Eocene volcanic rocks include trachyandesite, dacite and rhyolite, which extend beyond the mineralized zone. Crystal tuffs are the main host rock of the Lubin-Zardeh Au-Cu ± Pb ± Zn deposit (Zamanian et al., 2019). Considering the close temporal and spatial association of the quartz-monzonite intrusions with epithermal mineralization, it may be inferred that these intrusions are genetically related to the epithermal mineralization at Lubin-Zardeh. Tectonic structures in the study area include folds and faults. The compressional forces in the Oligocene have resulted in folding and extensive fractures. The formation of these fractures has created open spaces as the conduit for hydrothermal solutions (Yasami et al., 2017). The presence of ore-bearing zones, the same trend with the fault zones, indicate that mineralization is controlled by fault systems. Two types of faults with the NE-SW (strike-slip fault) and E-W (normal fault) trends have been expanded parallel and perpendicular to the axis of the fold. The quartz monzonite intrusions associated with Au-Cu ± Pb ± Zn mineralization at Lubin-Zardeh were emplaced in strike-slip and normal fault zones (Yasami et al., 2017).

2.3. Petrography

The Lubin-Zardeh pluton is one of the largest intrusive bodies within the TMB and forms a 20–30 km long elongated NW-SE trending intrusion composed of several monzodiorite, monzonite, quartz monzonite intrusions. The latest magmatic phases are represented by monzogranite and aplite dykes, which cross-cut the quartz monzonites. Rocks of the Lubin-Zardeh pluton are mainly medium to coarse grained with porphyritic to granular textures, with local variations in texture and mineral assemblage (Moayyed, 2001).

Quartz monzodiorite is generally medium-grained and characterized by an equigranular texture, comprising plagioclase (60–64%), K-feldspar (25–27%), quartz (7–10%) and clinopyroxene (8–11%). Accessory minerals include zircon, magnetite, apatite and minor titanite. Plagioclase occurs as large, euhedral to subhedral crystals. Clinopyroxene is subhedral and was altered to chlorite and amphibole in some samples. The quartz-monzodiorites show a granophytic texture that contains quartz and K-feldspar in characteristic angular intergrowths (Moayyed, 2001).

Monzonite constitutes of major minerals, e.g., plagioclase (30–35%), K-feldspar (25–30%), amphibole (10–15%), and accessory minerals of biotite, titanite, apatite, zircon, pyrite, and secondary goethite. In the more siliceous quartz-bearing monzonites, the dominant ferromagnesian constituents are biotite and hornblende. Monzonite porphyries carry phenocrysts of plagioclase with andesine cores and outer zones of oligoclase, which in turn may be enveloped in alkali feldspar. K-

feldspar may also have been observed as phenocrysts, but large ferromagnesian crystals are rare. The groundmass consists of sodic plagioclase and orthoclase interlocking, which stippled with augite, hornblende, biotite, opaque oxides, apatite, and titanite (Moayyed, 2001).

Quartz monzonite body forms a large part of the Tarom intrusive complex. The prevailing texture is granular and granophytic texture. The granophytic and porphyry granular textures indicate moderately low depth of emplacement of these bodies. These rocks are generally medium grained, comprised of plagioclase (35–40%), K-feldspar (35–40%), clinopyroxene (7–10%), amphibole (7–10%), biotite (4–6%), quartz (5–10%). Accessory minerals include zircon, magnetite, apatite and titanite (Moayyed, 2001).

Monzogranite and granitic rocks include of amphibole, biotite, plagioclase, alkali-feldspar and quartz as major minerals. Accessory minerals are zircon, monazite, apatite, magnetite and titanite. Electron microprobe and reflective light microscope studies show that idiomorphic crystals of magnetite are also abundant in these rocks (Nabatian et al., 2014).

Eocene volcanoclastic units in the studied area are divided to Amand and Kordkand formations. The lower part of the Kordkand Formation, which was studied in this area, is comprised of crystal tuff and tuffaceous sandstone (Amini et al., 2001). The tuffs have dacitic and rhyolitic composition and consist of plagioclase, K-feldspar, quartz, biotite and amphibole. Plagioclase, K-feldspar, biotite and amphibole are medium-grained minerals with anhedral to subhedral shapes (Hirayama et al., 1966).

Volcanic rocks of the investigated area consist of trachyandesite lavas. The trachy-andesites show greenish gray to pink with microlitic porphyry texture. Plagioclase, biotite and K-feldspar are the major constituents and accessory minerals are quartz and opaque minerals. Trachyandesite contains phenocrysts of plagioclase, K-feldspar, sardine, hornblende ± biotite ± augite ± quartz ± Fe-Ti oxide ± apatite in a fluidal microlithic groundmass (Moayyed, 2001).

3. Methodology

Samples were collected for chemical analysis within the study area. A total of 30 samples of intrusive rocks (Table 1), and 15 samples of volcanic rocks (Table 2) were analyzed in the Geological Survey of Iran for major oxides by X-ray fluorescence (XRF; Philips, magix-pro, pw 2540 equipped with standardless IQ + software) and trace elements by Inductively Coupled Plasma (ICP) Optical Emission Spectrometer (Varian, 735-ES, with standard stream sediment reference material; detection limit for trace elements 0.1–0.5 ppm). A total of 45 thin sections from host rock (volcanoclastic and intrusive rocks) were studied by optical microscopy.

A total of 21 samples were analyzed for Sr and Nd isotopes of the whole rock using the routine column chemistry separation and mass spectrometric methods (Table 3). Furthermore, 18 samples were analyzed for Pb isotopes of the whole rock samples using a multi-collector inductively coupled plasma mass spectrometer (MC-ICP-MS) (Table 4). Isotopic analyses of Sr, Nd and Pb were carried out at the State Key Laboratory for Mineral Deposits Research at Nanjing University in China.

4. Geochemistry of igneous rocks

The results of whole rock geochemical analyses of Lubin-Zardeh plutonic and volcanic rocks are presented in Tables 1 and 2. The Lubin-Zardeh intrusive rocks have SiO₂ ranging from 56.0 to 74.2 wt% and Al₂O₃ from 12.4 to 19.5 wt%. Their Na₂O contents range from 1.4 to 4.6 wt% and K₂O from 2.3 to 8.7 wt% with Ni ranging from 23 to 31 ppm and Cr from 44 to 87 ppm.

In the total alkali silica diagram (Cox et al., 1979), the Lubin-Zardeh intrusive samples were plotted mainly in the fields of monzodiorite, monzonite, quartz monzonite, and monzogranite (Fig. 2a) and volcanic

Table 1

Major oxides (wt. %) and trace elements (ppm) concentrations of the Lubin-Zardeh plutonic rocks.

Sample	Lithology	UTM (X, Y) WGS 84, Zone-39			SiO ₂	TiO ₂	Al ₂ O ₃	Fe ₂ O ₃	MnO	MgO	CaO	Na ₂ O	K ₂ O	P ₂ O ₅	LOI	Total	Ba		
GR-R-1	Monzogranite	E318235	N4070635	69.80	0.39	14.80	3.0	0.12	0.83	2.0	3.0	5.30	0.16	0.48	99.9	415			
GR-R-2	Monzogranite	E318235	N4070636	66.21	0.44	15.9	3.9	0.07	0.91	2.8	2.9	5.92	0.16	0.47	99.7	792			
GR-R-3	Monzogranite	E318235	N4070637	67.80	0.42	15.70	3.2	0.08	0.85	2.7	2.9	5.66	0.14	0.44	99.9	642			
mg-N-77	monzogranite	E319556	N4069769	69.00	0.37	15.40	3.0	0.11	0.86	2.2	3.7	5.08	0.12	0.12	100.0	581			
MD-N-4	Monzodiorite	E320506	N4069578	56.10	0.84	16.20	8.9	0.14	2.84	7.5	3.5	2.89	0.33	0.15	99.4	691			
MD-N-74	Monzodiorite	E320318	N4069348	56.40	0.75	16.50	8.4	0.14	2.72	6.6	3.1	4.06	0.34	0.51	99.6	681			
MD-N-89	Monzodiorite	E320250	N4069198	56.50	0.78	15.20	9.1	0.18	2.18	7.0	3.0	4.03	0.32	0.80	99.1	811			
MD-R-1	Monzodiorite	E320362	N4069038	56.00	0.78	17.50	8.6	0.13	2.67	7.4	2.8	2.95	0.30	0.42	99.6	761			
MD-R-2	Monzodiorite	E320331	N4068829	58.90	0.30	17.00	7.5	0.14	2.32	6.4	2.6	4.10	0.32	0.36	100.0	680			
MD-R-3	Monzodiorite	E317047	N4069075	58.00	0.68	16.00	8.5	0.16	2.74	6.9	2.6	3.71	0.28	0.43	100.0	742			
M-N-57	Monzonite	E318919	N4069341	59.40	0.57	17.8	4.1	0.16	2.47	6.4	3.8	4.80	0.08	0.72	99.6	581			
M-N-67	Monzonite	E318715	N4068966	57.88	0.90	18.75	5.2	0.14	2.46	6.2	3.1	4.33	0.36	0.43	99.6	561			
M-N-76A	Monzonite	E318640	N4068813	57.20	0.58	17.00	7.2	0.13	2.90	5.5	3.2	4.73	0.31	0.55	99.3	541			
M-N-81	Monzonite	E318516	N4068612	57.01	0.66	17.20	7.7	0.12	2.16	5.7	3.1	4.46	0.34	0.53	99.0	541			
M-N-87	Monzonite	E319811	N4068343	59.00	0.68	17.29	6.5	0.18	2.16	5.7	3.5	3.96	0.27	0.50	99.7	581			
M-N-92	Monzonite	E319857	N4069330	57.60	0.77	17.10	7.0	0.11	2.21	6.1	3.2	4.51	0.35	0.30	99.3	561			
MZ-R-1	Monzonite	E317123	N4069547	59.70	0.68	16.80	4.4	0.15	2.51	6.3	3.1	4.94	0.06	0.45	99.0	514			
MZ-R-2	Monzonite	E317105	N4069320	56.40	0.73	17.80	7.9	0.14	2.35	6.2	2.6	4.49	0.33	0.33	99.3	653			
MZ-R-3	Monzonite	E317047	N4069075	57.50	0.52	17.01	7.2	0.13	2.93	5.5	2.6	4.92	0.32	0.52	99.2	560			
MZ-R-4	Monzonite	E317006	N4068866	57.00	0.66	17.50	7.4	0.12	2.32	6.1	2.5	4.76	0.33	0.51	99.2	606			
MZ-R-5	Monzonite	E317396	N4068715	57.90	0.55	17.40	7.6	0.10	2.03	5.6	2.6	4.65	0.31	0.48	99.3	553			
MZ-R-6	Monzonite	E315558	N4070047	64.10	0.50	16.00	5.0	0.12	1.87	3.7	2.9	5.14	0.11	0.58	100.0	693			
MZ-R-7	Monzonite	E315535	N4069779	63.70	0.53	16.20	4.6	0.12	1.70	3.8	3.0	5.48	0.18	0.11	99.4	775			
MZ-R-8	Monzonite	E315331	N4069104	59.10	0.68	17.30	6.5	0.17	2.17	5.7	3.5	3.96	0.27	0.08	99.4	581			
MZ-R-9	Monzonite	E320781	N4067965	61.10	0.61	15.10	5.5	0.13	2.84	5.4	2.9	5.17	0.25	0.75	99.7	700			
QM-N-10	Quartz monzonite	E317000	N4067799	66.05	0.47	16.00	3.8	0.07	0.93	2.8	3.4	5.78	0.15	0.44	99.8	700			
QM-N-32	Quartz monzonite	E318018	N4068270	67.10	0.41	15.80	3.1	0.07	0.88	2.8	3.5	5.58	0.13	0.45	99.8	761			
QM-N-49	Quartz monzonite	E318292	N4068462	62.00	0.61	15.12	5.5	0.13	2.85	5.4	2.9	5.18	0.26	0.04	100.0	701			
QM-N-86	Quartz monzonite	E318949	N4068526	62.70	0.52	16.50	4.8	0.11	1.83	3.8	3.6	5.08	0.20	0.63	99.7	801			
QM-N-91	Quartz monzonite	E319449	N4068450	62.80	0.58	15.70	5.1	0.13	1.93	3.8	3.4	5.52	0.22	0.16	99.3	761			
Sample	Lithology	Rb	Sr	Cs	Ga	Ta	Nb	Hf	Zr	Y	Th	U	Cr	Ni	Co	V	Cu	Pb	
GR-R-1	Monzogranite	170	857	3.18	14.4	0.30	15.5	1.48	198	14.9	5.2	3.66	34.0	24.5	5.5	49.1	18.0	25.2	
GR-R-2	Monzogranite	187	271	2.13	15.5	0.62	18.0	0.76	241	13.7	7.6	3.57	31.4	26.1	5.8	59.0	13.0	21.0	
GR-R-3	Monzogranite	193	638	2.17	14.8	0.48	16.3	0.51	232	13.5	10.4	4.22	36.1	24.8	5.7	50.2	13.1	18.8	
mg-N-77	monzogranite	168	911	3.50	15.0	1.00	16.0	5.00	301	12.4	7.4	3.88	31.0	27.0	4.8	41.0	17.0	12.0	
MD-N-4	Monzodiorite	71	781	2.00	19.0	0.50	10.0	5.00	131	12.4	5.0	1.29	37.0	25.0	20.1	182.0	54.0	33.0	
MD-N-74	Monzodiorite	133	771	4.30	16.0	0.89	19.1	4.80	151	14.2	7.2	2.27	37.0	25.0	21.8	177.0	109.0	43.0	
MD-N-89	Monzodiorite	125	561	5.00	18.0	0.60	12.0	6.00	221	13.2	8.0	2.23	35.0	20.0	15.0	172.0	49.0	23.0	
MD-R-1	Monzodiorite	80	833	1.92	18.2	0.75	9.2	1.36	134	14.5	4.2	1.12	37.4	25.3	20.1	198.0	57.0	7.0	
MD-R-2	Monzodiorite	137	592	4.39	17.6	0.50	16.4	0.42	181	17.4	8.5	2.27	62.2	21.5	19.8	163.0	54.0	17.5	
MD-R-3	Monzodiorite	122	977	3.76	17.4	0.80	12.2	0.52	161	11.4	6.0	6.62	62.4	26.2	21.2	173.0	65.0	15.5	
M-N-57	Monzonite	143	721	2.30	20.0	0.80	11.0	8.00	231	11.7	14.7	3.10	33.0	31.0	12.4	112.0	22.0	20.0	
M-N-67	Monzonite	148	881	4.20	18.0	0.31	12.0	7.10	281	11.2	13.7	4.67	51.0	24.0	21.1	165.0	85.0	22.0	
M-N-76A	Monzonite	181	651	7.61	17.2	0.41	14.1	6.20	221	11.2	18.1	5.47	34.0	27.0	16.4	136.0	71.0	15.0	
M-N-81	Monzonite	175	851	5.20	18.0	0.80	15.0	9.00	281	12.8	19.8	6.46	42.0	29.0	17.9	146.0	61.0	19.0	
M-N-87	Monzonite	131	611	3.10	16.0	0.90	15.0	5.00	161	11.7	13.5	5.05	36.0	28.0	15.5	119.0	56.0	7.0	
M-N-92	Monzonite	154	381	4.70	16.0	0.40	13.0	8.00	261	16.0	15.6	4.14	36.0	22.0	14.8	146.0	74.0	16.0	
MZ-R-1	Monzonite	125	944	1.82	17.2	0.65	12.6	1.02	227	6.9	13.3	1.87	44.2	23.2	11.2	97.6	65.0	21.8	
MZ-R-2	Monzonite	160	734	4.02	19.0	0.41	18.8	1.12	242	13.8	16.4	4.64	67.8	23.8	20.8	177.0	54.0	15.9	
MZ-R-3	Monzonite	178	950	6.07	17.1	0.45	11.2	0.55	232	12.4	17.7	4.30	49.2	26.8	16.3	148.0	54.1	18.5	
MZ-R-4	Monzonite	167	878	4.35	17.2	0.62	10.7	1.30	267	18.5	18.7	3.73	66.4	23.2	15.7	174.0	45.0	13.9	
MZ-R-5	Monzonite	188	467	4.81	17.4	0.85	14.1	0.88	284	10.3	21.4	5.60	56.3	22.0	19.7	164.0	48.0	14.7	
MZ-R-6	Monzonite	135	753	3.20	15.1	0.60	15.8	0.37	211	9.5	16.3	3.22	36.7	21.0	8.5	94.2	62.0	22.4	
MZ-R-7	Monzonite	167	493	3.82	15.7	0.48	17.3	0.56	244	11.6	19.7	3.35	35.6	20.2	8.3	93.4	70.0	23.2	
MZ-R-8	Monzonite	130	510	3.20	15.0	0.80	14.0	4.00	160	11.8	13.4	5.06	31.0	27.0	15.5	117.0	56.0	14.6	
MZ-R-9	Monzonite	183	741	3.70	15.0	0.70	17.0	7.00	241	6.4	17.4	3.83	31.0	21.0	9.2	132.0	68.0	30.0	
QM-N-10	Quartz monzonite	171	481	2.10	15.0	0.50	11.0	7.00	251	7.3	5.6	4.96	38.0	26.0	5.0	54.0	12.0	13.0	
QM-N-32	Quartz monzonite	177	540	2.30	15.0	0.50	13.0	8.00	250	11.8	5.0	4.32	39.0	24.0	5.2	46.0	12.0	16.0	
QM-N-49	Quartz monzonite	184	741	3.80	17.0	0.51	17.0	7.00	241	11.5	5.7	3.82	43.0	20.0	9.3	133.0	15.0	8.0	
QM-N-86	Quartz monzonite	134	501	3.90	16.0	0.80	18.0	7.00	231	10.7	15.1	3.81	35.0	21.0	7.2	75.0	11.0	14.0	
QM-N-91	Quartz monzonite	156	461	5.00	16.0	0.50	18.0	7.00	231	10.1	6.5	3.92	31.0	22.0	7.0	84.0	12.0	12.0	
Sample	Lithology	Zn	Sn	W	Mo	La	Ce	Pr	Nd	Sm	Eu	Gd	Tb	Dy	Ho	Er	Tm	Yb	Lu
GR-R-1	Monzogranite	57	2.0	2	2	24.7	59	5.74	20.8	4.32	0.79	4.21	0.67	3.20	0.91	2.54	0.44	1.85	0.41
GR-R-2	Monzogranite	45	2.0	4	2	36.0	68	7.45	26.4	5.00	0.93	4.61	0.71	3.13	0.88	2.44	0.41	1.80	0.30
GR-R-3	Monzogranite	51	2.0	3	3	29.													

Table 1 (continued)

Sample	Lithology	Zn	Sn	W	Mo	La	Ce	Pr	Nd	Sm	Eu	Gd	Tb	Dy	Ho	Er	Tm	Yb	Lu
MD-R-2	Monzodiorite	86	2.0	6	3	28.0	56	6.58	25.3	5.27	1.32	5.02	0.77	2.35	0.93	2.47	0.37	1.44	0.36
MD-R-3	Monzodiorite	64	2.0	4	3	29.4	58	6.85	26.6	5.56	1.51	5.36	0.70	2.63	0.97	2.51	0.38	1.44	0.35
M-N-57	Monzonite	57	2.0	2	3	20.6	43	5.90	23.8	5.90	1.37	6.18	1.04	3.65	1.30	3.64	0.57	1.88	0.63
M-N-67	Monzonite	50	2.0	1	4	27.3	56	6.82	26.8	5.70	1.19	5.59	0.81	3.64	0.94	2.77	0.42	1.60	0.36
M-N-76A	Monzonite	77	3.0	5	3	34.1	67	8.02	29.8	5.91	1.21	5.91	0.88	3.64	0.98	2.87	0.38	1.80	0.37
M-N-81	Monzonite	50	2.0	6	3	36.6	73	8.60	31.6	6.30	1.12	6.35	0.94	2.22	0.97	2.77	0.45	1.90	0.45
M-N-87	Monzonite	95	1.0	4	2	27.9	55	6.08	25.0	4.80	1.14	5.04	0.76	1.20	0.83	2.55	0.38	1.60	0.35
M-N-92	Monzonite	33	2.0	6	3	32.0	62	7.58	27.6	5.40	1.23	5.91	0.92	1.63	0.95	2.77	0.42	1.80	0.36
MZ-R-1	Monzonite	68	1.0	5	2	17.6	38	4.92	20.2	5.17	1.25	5.37	0.85	3.32	1.15	3.30	0.55	1.45	0.52
MZ-R-2	Monzonite	64	1.0	4	2	26.8	54	6.58	25.8	5.70	1.30	5.54	0.86	1.96	1.06	2.78	0.45	0.81	0.42
MZ-R-3	Monzonite	79	1.0	7	2	30.8	63	7.30	27.5	5.67	1.22	5.39	0.80	3.68	1.02	2.65	0.44	1.72	0.39
MZ-R-4	Monzonite	37	1.0	2	2	34.2	68	8.06	30.1	6.23	1.30	5.89	0.88	1.14	1.10	2.91	0.46	0.95	0.43
MZ-R-5	Monzonite	55	1.0	1	2	36.5	73	8.30	31.4	6.42	1.23	6.00	0.91	1.28	1.13	2.97	0.48	0.97	0.42
MZ-R-6	Monzonite	53	1.0	3	2	20.8	45	5.43	20.8	4.36	1.07	4.16	0.65	3.84	0.83	2.23	0.36	1.36	0.35
MZ-R-7	Monzonite	58	2.0	3	2	31.1	57	6.57	24.2	4.68	0.97	4.34	0.66	3.76	0.81	2.10	0.34	1.29	0.33
MZ-R-8	Monzonite	97	1.0	2	2	27.9	54	6.09	24.0	4.80	1.14	5.04	0.77	3.10	0.82	2.56	0.38	1.60	0.34
MZ-R-9	Monzonite	45	1.0	2	2	26.8	46	5.27	20.1	4.40	0.91	4.02	0.60	3.76	0.81	2.32	0.32	1.40	0.32
QM-N-10	Quartz monzonite	39	2.0	4	3	38.1	69	7.45	26.2	5.00	0.91	4.84	0.74	3.19	0.83	2.58	0.42	1.10	0.37
QM-N-32	Quartz monzonite	40	2.0	4	3	30.4	57	6.49	23.1	4.50	1.00	4.51	0.67	3.73	0.78	2.37	0.38	1.70	0.38
QM-N-49	Quartz monzonite	45	2.0	1	3	26.8	46	5.27	20.1	4.40	0.91	4.02	0.60	3.76	0.82	2.31	0.33	1.40	0.31
QM-N-86	Quartz monzonite	52	2.0	4	2	20.8	43	5.24	20.6	4.00	1.08	4.39	0.67	3.67	0.72	2.16	0.36	1.40	0.32
QM-N-91	Quartz monzonite	57	2.0	6	3	32.0	59	6.49	24.6	4.50	0.90	4.53	0.68	3.56	0.73	2.11	0.35	1.50	0.33

rocks samples were plotted within the field of dacite, rhyolite, and trachyandesite boundary (Fig. 2b). Based on the Th/Yb versus Ta/Yb (Condie, 1989) diagram, the Lubin-Zardeh samples were plotted in the field of high-K calc-alkaline (shoshonite) field (Fig. 2c).

Using A/CNK versus A/NK diagram of Maniar and Piccoli (1989), the Lubin-Zardeh samples are plotted mainly in the field of metaluminous (Fig. 2d) that can be attributed either to the differentiation of hornblende or water content in the melting zone (Zen, 1986; Waight et al., 1998). However, the mineralogy of the Lubin-Zardeh samples, that include biotite, hornblende, magnetite, apatite and zircon, absence of Al rich mineral such as cordierite, corundum, topaz as well as lack of crustal enclaves' points to their metaluminous nature. The SiO₂ content, molecular A/CNK ratio, K₂O/Na₂O ratio, main modal minerals (such as hornblende and biotite), and chemical composition of Lubin-Zardeh samples all confirm their I-type characteristics (Harris et al., 1986).

In addition, all samples exhibit high Sr (425–1150 ppm), and low Y (5–15 ppm), and Yb (1–1.98 ppm) contents resulting in high Sr/Y (20–188 ppm) and La/Yb (11–78.4 ppm), jointly indicating that the studied intrusions can be classified having an adakitic affinity. Also, high Zr/Sr (14–127 ppm) ratios are also comparable with modern adakites (Foley et al., 2002). Moreover, the adakitic affinity of the studied rocks becomes apparent in the Sr/Y vs. Y discrimination diagram (Defant and Drummond, 1990; Fig. 2e). Discriminating features of adakite magmas have been used to trace magma sources with the presence of garnet and rutile and in the absence of plagioclase (Chung et al., 2003; Rapp and Watson, 1995; Rapp et al., 1991; Fu et al., 2012).

The aforementioned geochemical features are compatible with the shoshonitic series, based on the classification of Peccerillo and Taylor (1976), Pearce (1982), and Liegeois et al. (1998; not shown). Therefore, a suitable petrogenetic model for these granitoids must reconcile both adakitic and shoshonitic affinities of the studied intrusion.

In the NMORB-normalized multi-element spider diagram (Sun and McDonough, 1989; Fig. 3a), all samples are enriched in LILEs and depleted in HFSEs, with pronounced negative anomalies of Nb, P, and Ti and positive anomalies of Sr. These features are typical of the subduction-related magmas, namely in the calc-alkaline volcanic arcs of continental active margins (e.g., Pearce, 1983; Wilson, 1989). The chondrite-normalized REE patterns (Sun and McDonough, 1989) of the studied intrusion (Fig. 3b) are enriched in the LREEs relative to the HREEs with (La/Yb)_N ranging from 7.4 to 16.7 and weak Eu anomaly. The volcanic and volcanioclastic rocks in the study area have somehow similar nature to the intrusive rocks. The negligible differences are due to development of strong alterations of volcanic and volcanioclastic

rocks (Fig. 4a, b).

5. Radiogenic isotope geochemistry

Sr-Nd isotopic compositions were determined for 21 whole-rock samples as well as Pb isotopic compositions for 18 samples, which are presented in Tables 3 and 4. Considering ages of 36 Ma for the studied intrusion, the calculated initial ⁸⁷Sr/⁸⁶Sr ratios range between 0.70476 and 0.70518; the initial ¹⁴³Nd/¹⁴⁴Nd ratios (t = 36 Ma) vary from 0.51263 to 0.51272 and are relatively homogeneous. In the Nd-Sr isotope diagram (Fig. 5), all the studied granitoid samples plot in the center of the diagram, in the field of underplated thick lower crust-derived adakitic rocks, e.g., Separation Point Batholith of New Zealand (Muir et al., 1995), delaminated lower crust-derived adakitic rocks (Wang et al., 2006b). They also have much lower εNd(t) than those of 400–179 Ma MORB (Mahoney et al., 1998; Tribuzio et al., 2004; Xu et al., 2003; Xu and Castillo, 2004) and Cenozoic adakites formed by slab melting (Aguillon-Robles et al., 2001; Kay et al., 1993; Wang et al., 2006b).

Initial ⁸⁷Sr/⁸⁶Sr and ¹⁴⁴Nd/¹⁴³Nd ratios are calculated adopting the zircon U-Pb age of 36 Ma obtained (Nabatian et al., 2016). The initial ⁸⁷Sr/⁸⁶Sr or I_{Sr} (t = 36 Ma) and Nd(t) (t = 36 Ma) values of the Lubin-Zardeh pluton span a range of 0.70476 to 0.7051 and 0.39 to 2.10, respectively (Table 3). All the isotopic data were plotted well above left quadrant of a conventional Sr-Nd isotope diagram (Fig. 5), where they were plotted close to the Tarom intrusions, Eocene Urumieh-Dokhtar rocks from the Khalkhab granitoid (Rezaei-Kahkhaei et al., 2011), Oligocene plutons from the southeastern part of the Urumieh-Dokhtar arc segment with porphyry copper mineralizations (Shafiei et al., 2009), the Sisdag pluton from the eastern Pontides in Turkey (Karsli et al., 2012), and adakitic rocks in the Dexing area (South China; Wang et al., 2006b). The single-stage (depleted mantle) Nd model ages (TDM) of the samples are relatively young and range from 0.69 to 1.06 Ga.

The host rock samples are relatively homogeneous in Pb isotopic compositions. Lead isotopic ratios of the samples are initial ²⁰⁶Pb/²⁰⁴Pb = 18.49–18.68, initial ²⁰⁷Pb/²⁰⁴Pb = 15.58–15.61, initial ²⁰⁸Pb/²⁰⁴Pb = 38.33–38.77 (Table 4). All the samples plot between EM1 (enriched mantle with intermediate ⁸⁷Sr/⁸⁶Sr, low ¹⁴³Nd/¹⁴⁴Nd and low ²⁰⁶Pb/²⁰⁴Pb) and EMII (enriched mantle with high ⁸⁷Sr/⁸⁶Sr, intermediate ¹⁴³Nd/¹⁴⁴Nd and high ²⁰⁶Pb/²⁰⁴Pb; Stacey and Kramers, 1975; Zindler and Hart, 1986), but generally closer to EMII.

Pb isotope compositions of eighteen samples from ore-hosting granitoids show a narrow range of ²⁰⁶Pb/²⁰⁴Pb (18.52–18.60),

Table 2

Major (wt. %) and trace element (ppm) concentrations of the Lubin-Zardeh volcanic rocks.

Sample	Lithology	UTM (X, Y) WGS 84, Zone-39	SiO ₂	TiO ₂	Al ₂ O ₃	Fe ₂ O ₃	MnO	MgO	CaO	Na ₂ O	K ₂ O	P ₂ O ₅	LOI	total	Ba	Rb				
V-rh-13	Rhyolite	E319964	N4070044	68.40	0.67	14.10	3.6	0.07	0.85	2.90	3.42	5.51	0.15	0.22	99.90	929	175			
V-rh-14	Rhyolite	E314073	N4064375	69.91	0.39	17.80	1.6	0.00	0.14	0.24	1.36	8.32	0.05	0.18	100.00	304	222			
V-rh-15	Rhyolite	E320859	N4069539	70.00	0.42	14.75	2.3	0.14	0.90	1.10	3.19	6.38	0.12	0.19	99.45	387	335			
V-rh-16	Rhyolite	E316331	N4067608	72.25	0.33	13.00	2.0	0.03	1.13	1.61	3.17	6.12	0.07	0.25	100.00	252	257			
V-rh-18	Rhyolite	E315656	N4067282	71.28	0.17	14.43	2.4	0.06	0.83	2.08	4.33	3.32	0.09	0.20	99.16	650	160			
V-rh-19	Rhyolite	E315538	N4065852	73.28	0.40	14.80	1.2	0.04	0.22	2.72	3.54	3.55	0.04	0.16	99.95	242	210			
V-rh-32	Rhyolite	E320261	N4066701	73.87	0.35	13.40	1.7	0.05	0.62	0.97	4.61	4.08	0.05	0.18	99.91	159	333			
V-rh-33	Rhyolite	E314476	N4065709	74.16	0.37	12.70	2.2	0.05	0.67	1.85	4.56	2.61	0.07	0.32	99.53	174	311			
V-Da-34	Rhyolite	E316461	N4067369	73.58	0.32	12.40	1.9	0.05	1.42	0.88	3.46	5.87	0.07	0.04	99.98	243	259			
V-Da-8	Dacite	E316826	N4066986	63.48	0.50	17.40	5.3	0.11	2.00	4.73	2.35	3.72	0.26	0.00	99.85	660	176			
V-Da-9	Dacite	E315252	N4065150	63.94	0.71	16.35	3.8	0.24	0.64	4.49	3.37	5.73	0.17	0.23	99.66	1042	176			
V-Da-NT1	Dacite	E320469	N4066267	64.35	0.49	17.53	3.6	0.08	1.01	4.42	3.56	3.98	0.13	0.14	99.26	778	115			
V-Da-NT2	Dacite	E315165	N4066267	64.67	0.51	17.56	3.6	0.08	1.05	4.39	3.59	3.94	0.17	0.16	99.76	812	118			
V-Da-NT6	Dacite	E315530	N4070981	62.53	0.45	19.53	3.3	0.07	0.95	5.67	3.69	3.23	0.14	0.33	99.88	590	210			
V-Da-NT7	Dacite	E320283	N4065575	64.27	0.52	17.72	3.8	0.07	1.08	4.54	3.63	3.83	0.17	0.16	99.78	781	106			
V-rh-13	Sr	Cs	Ga	Ta	Nb	Hf	Zr	Y	Th	U	Cr	Ni	Co	V	Cu	Pb	Zn	Sn	W	Mo
V-rh-14	647	2.60	16.00	0.80	18.0	11.00	320	14.0	11.00	2.00	39.0	24.0	9.00	62.0	3.0	11.0	34.0	1.0	0	2
V-rh-15	872	3.70	16.00	0.98	19.0	8.00	341	12.0	18.00	7.00	52.0	21.0	4.00	28.0	1.0	32.0	10.0	1.0	2	2
V-rh-16	544	4.00	18.00	0.69	19.0	14.00	394	7.0	14.00	6.00	87.0	20.0	6.00	22.0	2.0	47.0	80.0	2.0	1	3
V-rh-18	626	2.70	17.00	0.53	17.0	8.00	222	15.0	8.00	2.00	30.0	22.0	4.00	24.0	2.0	11.0	32.0	1.0	2	3
V-rh-19	970	1.30	15.00	0.67	16.0	10.00	68	6.0	10.00	3.00	38.0	26.0	2.00	36.0	4.30	13.0	15.0	2.0	2	3
V-rh-32	1074	1.34	16.70	0.78	15.0	15.00	295	7.0	9.00	15.00	34.0	22.0	2.00	21.0	4.0	26.0	24.0	3.0	7	4
V-rh-33	1150	2.80	16.60	0.75	15.0	13.00	324	7.0	12.00	4.00	41.0	25.0	3.00	14.0	1.0	17.0	39.0	3.0	9	4
V-Da-34	929	2.31	19.10	0.81	13.3	13.00	324	12.0	4.00	8.00	59.0	21.0	1.00	26.0	4.0	21.0	41.0	1.0	3	2
V-Da-8	475	2.70	19.20	0.38	18.0	7.00	214	11.0	5.00	3.00	35.0	28.0	7.00	47.0	12.0	16.0	28.0	2.0	1	3
V-Da-9	941	2.50	17.00	0.52	15.0	8.00	251	5.0	3.00	0.00	64.0	21.0	8.00	121.0	10.0	25.0	57.0	1.1	6	2
V-Da-NT1	791	3.00	16.00	0.52	19.0	9.00	284	9.0	10.00	5.00	34.0	26.0	16.00	99.0	12.0	18.0	67.0	1.0	3	2
V-Da-NT2	894	2.40	17.00	0.80	14.0	5.80	223	6.6	13.20	4.30	43.2	22.1	5.00	52.7	31.1	15.0	45.7	1.0	5	2
V-Da-NT6	788	2.60	15.00	0.80	13.2	5.60	218	7.0	12.30	2.70	44.6	22.8	5.80	53.7	19.0	18.3	51.8	1.0	7	3
V-Da-NT7	425	1.31	18.00	0.70	11.0	4.51	200	10.0	12.00	3.12	42.6	22.0	5.30	46.5	24.0	16.9	40.5	1.0	1	2
V-rh-13	La	Ce	Pr	Nd	Sm	Eu	Gd	Tb	Dy	Ho	Er	Tm	Yb	Lu						
V-rh-14	36.0	68	5.60	22.3	4.80	1.10	4.70	0.75	3.41	0.91	2.72	0.42	1.30	0.28						
V-rh-15	64.0	41	5.70	24.0	5.10	1.30	4.90	0.60	3.20	0.80	2.50	0.30	1.51	0.28						
V-rh-16	25.6	50	5.80	24.3	3.10	1.10	4.80	0.51	3.70	1.10	0.80	0.10	1.32	0.10						
V-rh-18	51.0	48	5.80	24.0	4.90	1.40	4.70	0.70	3.50	1.10	3.20	0.40	1.12	0.27						
V-rh-19	45.0	80	5.60	20.0	5.00	1.50	6.00	0.75	3.30	0.90	2.40	0.43	1.98	0.32						
V-rh-32	87.0	51	5.80	13.0	3.20	1.60	5.60	1.15	3.20	1.32	3.40	0.43	1.11	0.32						
V-rh-33	60.0	99	5.80	23.2	5.10	1.08	4.90	0.90	3.80	1.00	2.90	0.47	1.90	0.30						
V-Da-34	48.0	71	7.00	31.0	6.80	1.80	4.70	1.10	3.20	0.90	3.80	0.60	1.00	0.34						
V-Da-8	54.0	65	5.90	24.1	6.80	1.80	4.80	0.70	2.90	0.90	3.70	0.60	1.90	0.29						
V-Da-9	62.0	25	5.70	22.5	4.80	1.30	4.80	0.80	3.30	1.00	2.70	0.50	1.13	0.33						
V-Da-NT1	32.0	32	5.80	22.6	4.90	1.40	4.90	0.80	3.40	0.90	2.80	0.40	1.90	0.40						
V-Da-NT2	25.7	50	5.60	22.4	4.70	1.20	4.70	0.70	2.20	0.90	2.60	0.40	1.70	0.40						
V-Da-NT6	26.0	51	5.70	23.1	4.90	1.20	4.80	0.70	2.40	0.90	2.70	0.40	1.80	0.40						
V-Da-NT7	23.1	43	4.90	19.5	4.10	1.30	4.00	0.60	3.60	0.70	2.20	0.30	1.30	0.40						

²⁰⁷Pb/²⁰⁴Pb (15.58–15.64), and ²⁰⁸Pb/²⁰⁴Pb (38.57–38.80) ratios. Most Pb isotope values of the ore-hosting granitoids plot close to the orogen curves at ²⁰⁷Pb/²⁰⁴Pb vs. ²⁰⁶Pb/²⁰⁴Pb and ²⁰⁸Pb/²⁰⁴Pbvs. ²⁰⁶Pb/²⁰⁴Pb diagrams of Doe and Zartman (1979) (Fig. 6a, b). The Pb isotope compositions of ore-hosting granitoids are relatively uniform, slightly radiogenic, and diagnostic of orogenic Pb isotope signatures (Doe and Zartman, 1979).

6. Geological characteristics of the deposit

6.1. Characteristics of the mineralized veins

The Lubin-Zardeh deposit consists of nine Cu-bearing quartz veins that occupy N15E-trending faults that cut in the late Eocene volcanoclastic (crystal tuff) and quartz- monzonite rocks (Fig. 7a-e). Base metal grades decrease gradually from the main quartz veins through stock-work quartz veinlets to argillic-altered wall-rock. The Lubin-Zardeh veins reach up to 1000 m in length and average 1.5 m in width, reaching a maximum of 3 m. They generally dip 60–70° SE with a known down-dip extension of about 70 m. Ore mineralization occur as

vein-veinlet, breccia cement, and disseminated grains (Fig. 7f-g).

The field evidences indicate the presence of silica-sulfide, silica-carbonate-sulfide, and carbonate vein-veinlets (Fig. 7a-c). Geometrically, these vein-veinlets occur in the vicinity of each other trending parallel and approximately parallel to the host fault zone. The veins have regular sharp contacts with host rocks, indicating that they formed by open-space filling. The veins are dominated by fine- to coarse-grained quartz crystals that locally reach 2 cm in size. Vug infill and comb textures have been observed in some samples; colloform and crustiform banding occurs commonly in the veins. Sulfide (pyrite, chalcopyrite, galena, and sphalerite) content of the veins and adjacent wall-rock locally exceeds 5%. Metal concentrations for outcrop samples average 1.3 wt% Cu, 0.7 wt% Pb, 0.4 wt% Zn and reaches up to 10 g/t Au (Zamanian et al., 2019). Some fractures are filled by carbonate during the post-ore stage, implying a successive re-opening of veins. Brecciation occurs regularly in the veins. Breccias are hydrothermally altered and clasts supported with abundant hydrothermal cement. Brecciation plays an important role in the formation of Lubin-Zardeh deposit and is characterized by in filling of sulfides into open spaces.

Table 3

Neodymium and strontium isotopic composition from the Lubin-Zardeh host rock.

Description	Sample No.	Rb (ppm)	Sr (ppm)	$^{87}\text{Rb}/^{86}\text{Sr}$	$^{87}\text{Sr}/^{86}\text{Sr}$	Sm (ppm)	Nd (ppm)	$^{147}\text{Sm}/^{144}\text{Nd}$	$^{143}\text{Nd}/^{144}\text{Nd}$	$^{87}\text{Sr}/^{86}\text{Sr}_i$ ($t = 36$ Ma)	ϵNd (0)	ϵNd (t)	T _{DM}
Quartz monzonite	GN-T01	36.3	232.1	0.4588	0.705286	3.65	17.68	0.1257	0.512719	0.705	1.6	2.1	747
Quartz monzonite	GN-T07	13.03	257.5	0.1484	0.70497	2.85	12.38	0.1398	0.512711	0.7048	1.4	1.86	906
Quartz monzonite	GN-T017	11.25	265.7	0.1242	0.704963	3.19	14.18	0.1368	0.51269	0.7049	1	1.47	912
Quartz monzonite	GN-T056	42.92	203.2	0.6194	0.705448	2.84	12.26	0.1405	0.512699	0.7051	1.2	1.62	941
Quartz monzonite	GN-T022	14.8	282.6	0.1536	0.705062	3.24	15.49	0.1272	0.512703	0.7049	1.3	1.77	788
Quartz monzonite	GN-T067	23.11	441	0.1536	0.704906	3.19	13.36	0.1449	0.512671	0.7048	0.6	1.07	1060
Quartz monzonite	GN-T081	17.79	327.3	0.1594	0.704985	3.06	14.86	0.1253	0.512703	0.7049	1.3	1.79	771
Quartz monzonite	GN-T012	38.65	218.6	0.5185	0.705384	3.04	17.29	0.1195	0.51271	0.7051	1.4	1.95	713
monzonite	GN-T038	30.2	262.2	0.3377	0.705323	4.41	22.6	0.1187	0.512655	0.7051	0.3	0.89	794
monzonite	GN-T042	25.09	274.7	0.2678	0.70532	4.2	20.75	0.123	0.512684	0.7051	0.9	1.42	784
monzonite	GN-T047	27.53	313.4	0.2576	0.704947	3.78	18.15	0.1265	0.512702	0.7048	1.2	1.75	784
monzonite	GN-T018	7.79	316.8	0.0721	0.704945	3.43	17.42	0.1197	0.512693	0.7049	1.1	1.62	742
monzonite	GN-T06	23.66	354.8	0.1955	0.705037	2.86	14.36	0.1212	0.512648	0.7049	0.2	0.73	828
monzonite	GN-T049	18.79	230	0.2396	0.70526	2.99	15.52	0.125	0.512661	0.7051	0.4	0.96	841
monzonite	GN-T043	22.79	297.7	0.2245	0.705191	3.97	19.39	0.1246	0.512669	0.705	0.6	1.12	824
monzonite	GN-T033	38.98	171	0.6684	0.705431	3.16	16.2	0.1185	0.512714	0.705	1.5	2.03	699
monzogranite	GN-T013	32.96	176.5	0.5476	0.705294	2.97	15.53	0.1161	0.512705	0.705	1.3	1.87	696
monzogranite	GN-T02	40.82	192.4	0.6221	0.705445	3.28	16.41	0.1215	0.512713	0.7051	1.5	2.01	722
monzodiorite	GN-T05	5.99	510	0.0345	0.704851	3.83	19.33	0.1203	0.51263	0.7048	-0.2	0.39	849
monzo diorite	GN-T04	17.87	406.4	0.129	0.704852	4.82	25.17	0.1164	0.512671	0.7047	0.6	1.21	751
monzodiorite	GN-T03	5.83	365.5	0.0468	0.704784	2.78	14.13	0.1195	0.512666	0.7047	0.5	1.09	784

6.2. Hydrothermal alteration

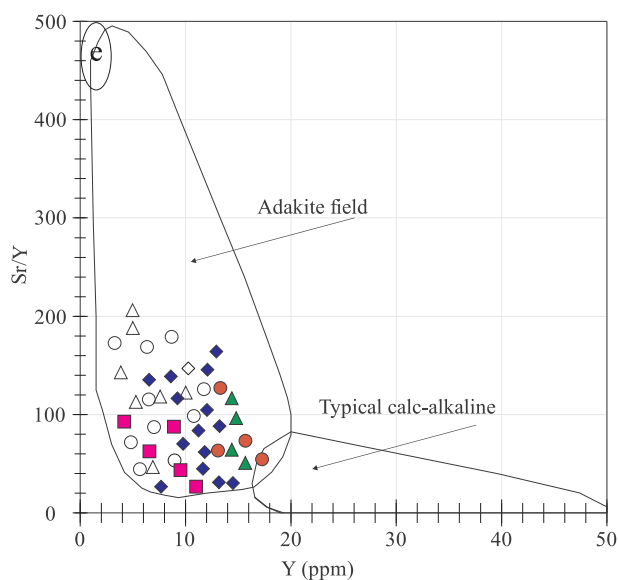
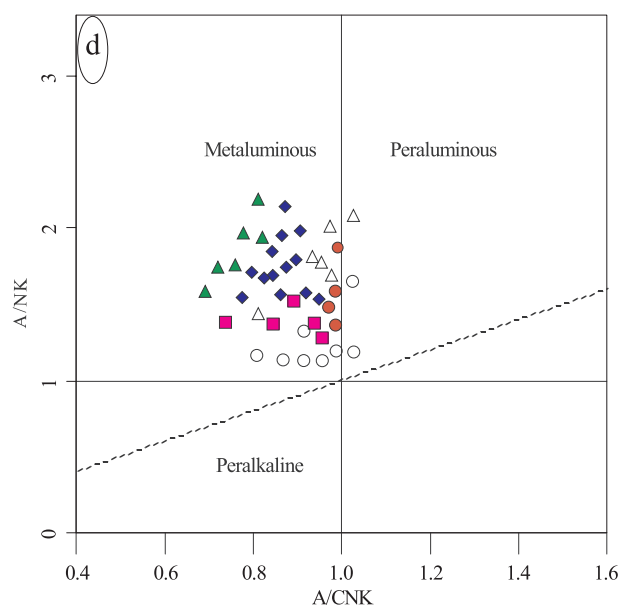
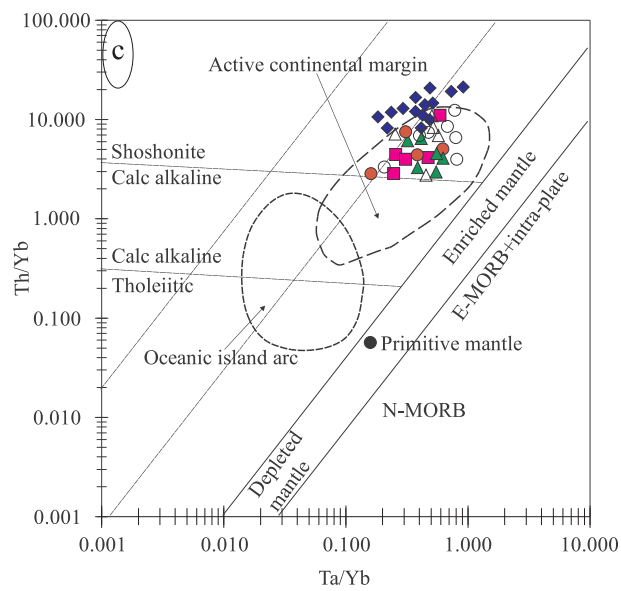
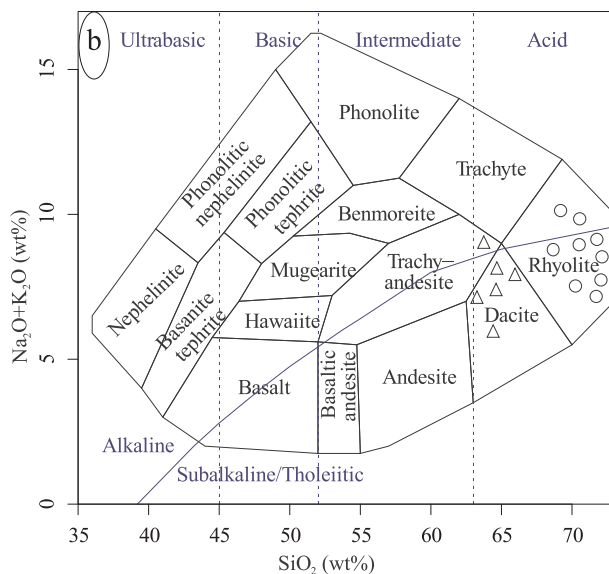
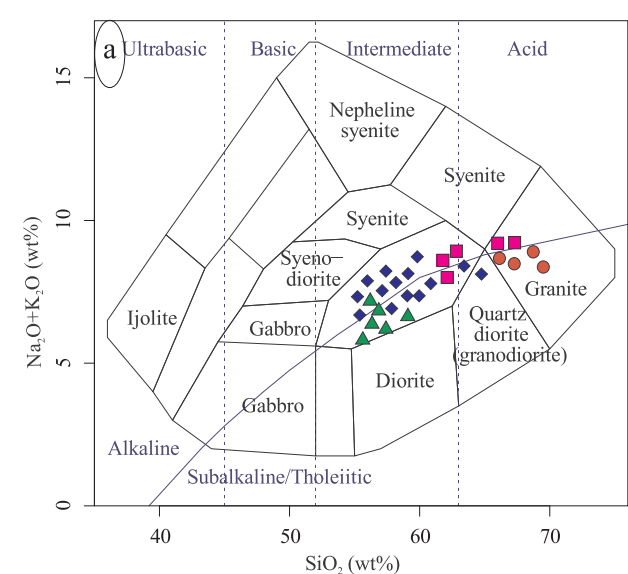
Detailed field geology and petrographic studies indicate that wall-rock alterations developed at the Lubin-Zardeh deposit include silicification, intermediate argillic, carbonate (Fig. 8a-c) and propylitic alteration; the silicification are closely related to the Au–Cu + Pb + Zn mineralization. The alteration styles show a systematic zonation pattern, from the silica, via intermediate argillic, to propylitic alteration. Silicification is the most common type of wall-rock alteration in the Lubin-Zardeh deposit. It is represented by pervasive addition of fine- to coarse-grained quartz into the host rocks to form massive siliceous rocks. Silicification is also associated with up to 5 cm width quartz veinlets that often contain variable amounts of sulfide minerals. High grade ore zones are mostly in the zones that have undergone significant silicification. The intermediate argillic alteration, with a width of about 3–5 m, is strongly fracture controlled and forms envelopes around the polymetallic quartz-sulfide veins. This alteration is mainly evident from replacement of plagioclase by sericite/illite, and minor amount of quartz, and calcite (Zamanian et al., 2019), and an associated change in color to yellow-green. As a result of the different degrees of hydrothermal alteration, the residual phenocrysts (pseudomorphs) of

plagioclase are generally retained. Sericite and illite are both related with low- to medium-temperature epithermal systems. Sericite generally forms at higher temperatures than illite, and is partially transformed to illite under epithermal conditions (e.g., Li et al., 2018). In the outer parts of the mineralized veins, the illite content associated with intermediate argillic alteration decreases with increasing sericite content. This indicates that at least some sericite may form earlier than illite and, therefore, that illite is an important index mineral for prospecting. Carbonate alteration is pervasive in the Lubin-Zardeh deposit, and can be divided into two types. The first type of calcite was closely related to silicification and is intergrown with quartz, forming polymetallic sulfide-quartz (platy calcite) veins (Zamanian et al., 2019). Consequently, this calcite associated with quartz formed in the main ore-forming stage. The second type of calcite is mostly evident as calcite veinlets that generally crosscut the quartz-sulfide veinlets, showing that these veinlets represent a late stage of alteration (Hosseinzadeh et al., 2014). Propylitic alteration is the most distal type of alteration that affects a variety of geological units. This alteration has typically weak to moderate intensity and generally is not texturally destructive. It is normally present in the form of the replacement of plagioclase, amphibole and pyroxene by chlorite-epidote-sericite-carbonate

Table 4

Lead isotopic composition from the Lubin-Zardeh host rock.

Description	Sample No.	U (ppm)	Th (ppm)	Pb (ppm)	$^{206}\text{Pb}/^{204}\text{Pb}$	$^{207}\text{Pb}/^{204}\text{Pb}$	$^{208}\text{Pb}/^{204}\text{Pb}$	$^{206}\text{Pb}/^{204}\text{Pb}$	$^{207}\text{Pb}/^{206}\text{Pb}$	$^{208}\text{Pb}/^{204}\text{Pb}$
Quartz monzonite	GN-T01	3.8500	11.5900	18.7300	18.7924	15.5896	38.7915	18.6500	15.5800	38.5600
Quartz monzonite	GN-T07	2.5200	9.8600	12.4800	18.7728	15.5960	38.7943	18.6600	15.5900	38.6200
Quartz monzonite	GN-T017	2.6200	9.5000	21.1700	18.7377	15.5866	38.7760	18.6200	15.5800	38.4600
Quartz monzonite	GN-T056	4.6500	15.9500	28.5800	18.7705	15.5901	38.8245	18.6400	15.5800	38.5700
Quartz monzonite	GN-T022	4.6400	8.6300	19.7900	18.7360	15.5858	38.7899	18.6000	15.5800	38.4700
Quartz monzonite	GN-T067	1.7100	5.6300	17.9100	18.7069	15.5912	38.7788	18.5700	15.5800	38.3300
Quartz monzonite	GN-T081	2.1200	8.6700	13.3500	18.7872	15.5918	38.8206	18.6800	15.5900	38.6000
Quartz monzonite	GN-T012	3.2200	12.0800	18.1800	18.7687	15.5877	38.8035	18.6500	15.5800	38.5900
monzonite	GN-T038	3.8100	7.6500	16.4700	18.7621	15.5909	38.7963	18.5400	15.5800	38.4900
monzonite	GN-T042	4.5100	9.1000	12.5100	18.8098	15.5952	38.8324	18.5900	15.5800	38.6400
monzonite	GN-T047	3.8100	8.0400	21.8700	18.7082	15.5928	38.7229	18.5000	15.5800	38.3400
monzonite	GN-T06	3.6000	7.3000	13.6500	18.7846	15.5949	38.8648	18.5700	15.5800	38.6000
monzonite	GN-T049	3.2000	4.6400	9.5200	18.7985	15.5939	38.8335	18.4900	15.5800	38.5400
monzonite	GN-T043	3.5500	6.5300	11.0700	18.8033	15.5941	38.8219	18.5600	15.5800	38.5800
monzogranite	GN-T013	1.4300	12.1300	17.7100	18.7370	15.5855	38.7884	18.6800	15.5800	38.5800
monzogranite	GN-T02	3.8100	18.5400	27.6600	18.7548	15.5905	38.8026	18.6600	15.5900	38.5900
monzodiorite	GN-T05	4.2400	16.0000	15.3200	18.7875	15.5984	38.9059	18.6700	15.5900	38.7700
monzodiorite	GN-T03	3.4100	8.6000	17.9900	18.7197	15.6173	38.8347	18.5400	15.6100	38.5400



(caption on next page)

Fig. 2. Classification of Lubin-Zardeh plutonic and volcanic rocks a. SiO_2 versus $\text{Na}_2\text{O} + \text{K}_2\text{O}$ binary diagram, plutonic rocks. b. SiO_2 versus $\text{Na}_2\text{O} + \text{K}_2\text{O}$ binary diagram, volcanic rocks. c. Plot of host rocks samples on Th/Yb versus Ta/Yb discrimination diagram of Pearce et al. (1984). d. Classification of the Lubin-Zardeh intrusive rocks in A/NK versus A/CNK diagram, Maniar and Piccoli (1989), ANK = molar $\text{Al}_2\text{O}_3/(\text{Na}_2\text{O} + \text{K}_2\text{O})$ and ACNK = molar $\text{Al}_2\text{O}_3/(\text{CaO} + \text{Na}_2\text{O} + \text{K}_2\text{O})$. e. Sr/Y versus Y discrimination diagram (Defant and Drummond, 1990) of studied samples. NMORB: N-type Mid-Ocean Ridge Basalts, E-MORB: E-type Mid-Ocean Ridge Basalts. Symbols as in Fig. 10d.

assemblages (Hosseinzadeh et al., 2014; Zamanian et al., 2019). Small amounts of quartz are present in the groundmass. In the outcrop, leached-oxidized zones are commonly focused along joints, fractures and faults. These zones are characterized by iron oxides-hydroxides, and copper, lead, and zinc carbonates, such as goethite, malachite, azurite, cerussite, and smithsonite.

6.3. Ore mineralogy

The hypogene ore assemblage of the Lubin-Zardeh deposit consists of chalcopyrite (more than 40 vol%), pyrite (less than 15 vol%), galena (less than 10 vol%) and sphalerite (less than 20 vol%) with supergene malachite, azurite, covellite, digenite, and goethite. The ore minerals occur as disseminated crystals, veinlets and as cement of hydrothermal breccias. Native gold, (Fig. 8d and e), occurs as anhedral grains (2–15 μm in size) associated with chalcopyrite-II in the open spaces of the quartz veins, which is consistent with the strong positive correlation of Cu and Au (Zamanian et al., 2019). SEM observations showed that native silver occurs as inclusions in the quartz gangue (Fig. 8f). Chalcopyrite, the main ore mineral in the deposit, typically occurs as disseminated, coarse-grained subhedral to anhedral crystals (up to 2 cm in size), or as massive aggregates in quartz veins and in the breccia cement. The first generation of chalcopyrite occurs as fine anhedral inclusions within sphalerite. Irregularly distributed small chalcopyrite inclusions with spherical or drop-like forms, known as “chalcopyrite disease” are observed in sphalerite (Sabeva et al., 2017; Fig. 8g and h). Chalcopyrite disease texture may be the result of replacement due to interaction of sphalerite with solutions, coprecipitation of sphalerite and chalcopyrite, crystal growth by solid-state diffusion and exsolution of CuS in Fe-bearing sphalerite. The main factors controlling these processes are the iron content of sphalerite, the volume relationships, temperature and the variations in sulfur fugacity (Barton and Bethke, 1987; Bente and Doering, 1993; Bonev and Radulova, 1994; Bortnikov et al., 1991; Wiggins and Craig, 1980). The second generation occurs as coarse-grained (30 to 400 μm) subhedral grains disseminated in the quartz vein (Fig. 8g and h).

Based on the mineralogy and texture studies, two pyrite generations are identified in the deposit. The first generation (Py-I) occurs as anhedral crystals along with sericitic alteration in the host rocks. The second generation (Py-II) and first generation of quartz are found as

disseminated fine grains in silica-sulfide vein-veinlets.

Sphalerite is also another ore mineral within the Lubin-Zardeh deposit. It occurs as optically clear honey colored variety, typically forming massive, coarse (generally greater than 5 mm in size) subhedral to anhedral grains. Sphalerite slightly post-dates chalcopyrite-II and galena but, in some cases, they are intergrown, indicating that all of these sulfides formed simultaneously. In some parts of the deposit, smithsonite replaces sphalerite along boundaries.

Galena with a massive or replacement texture accompanies sphalerite and covellite in the veins and veinlets. It usually replaces pyrite and chalcopyrite and is, in turn, replaced by sphalerite. In the main part of the ore zones, galena is replaced by cerussite.

Phases of tetrahedrite-tennantite (Td-Tn) were identified in most of the investigated samples, although the abundances and sizes of these phases are minor. It is observed that tetrahedrite-tennantite grains appear mostly associated with sphalerite, galena and chalcopyrite in quartz veins and veinlets.

The vein-veinlet gangue minerals in the Lubin-Zardeh deposit consist of quartz (more than 50 vol%), carbonates (calcite; more than 10 vol%), sericite (more than 10 vol%), clay (more than 10 vol%) and adularia (more than 5 vol%). Quartz is the most important gangue mineral within the Lubin-Zardeh deposit. It typically occurs as fine- to coarse-grained anhedral to euhedral crystals (< 200 μm up to 1 cm in size), or as massive aggregates in veins. Quartz usually shows comb and vug infill textures (Hosseinzadeh et al., 2014). In some parts of the ore zones, cockade, crustiform, colloform, and plumose structures are observed in quartz veins and breccia cements. Based on the mineralogical studies, two quartz generations are recognized. The first one consists of coarse-grained quartz that is cut by microcrystalline quartz. Early quartz usually shows comb and euhedral textures in equilibrium with base metals (chalcopyrite-I, sphalerite, galena; stage I). The second generation of quartz with microcrystalline and fine-grained textures (stage II) is in equilibrium with Au and sometimes minor chalcopyrite-II; Zamanian et al., 2019). The carbonate minerals (calcite and dolomite) at the Lubin-Zardeh deposit are formed in the pre-ore and post-ore stages. The carbonate minerals occurred as vein-veinlets.

Calcite is the second common gangue mineral at Lubin-Zardeh deposit. It usually infills cavities with quartz and sulfides, and shows colloform and bladed textures (Hosseinzadeh et al., 2014). Bladed calcite is usually replaced by quartz (Hosseinzadeh et al., 2014).

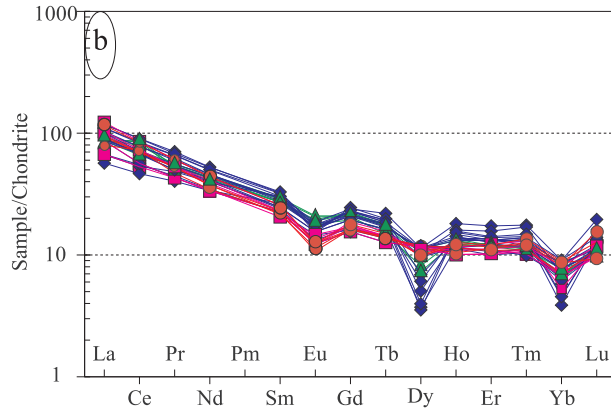
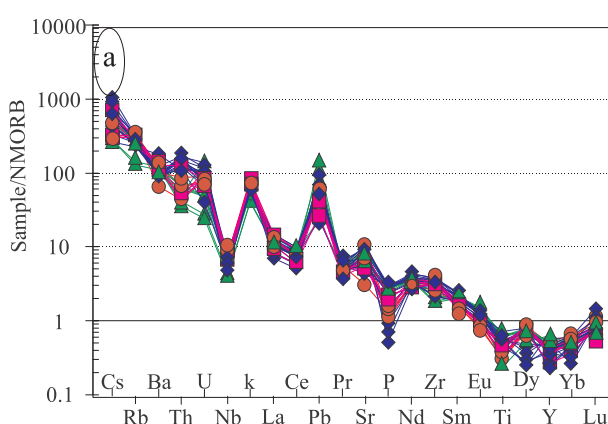


Fig. 3. a. NMORB-normalized trace element compositions. b. Chondrite-normalized REE patterns of the Lubin Zardeh plutonic samples (normalization factors from Sun and McDonough, 1989). Symbols as in Fig. 10d.

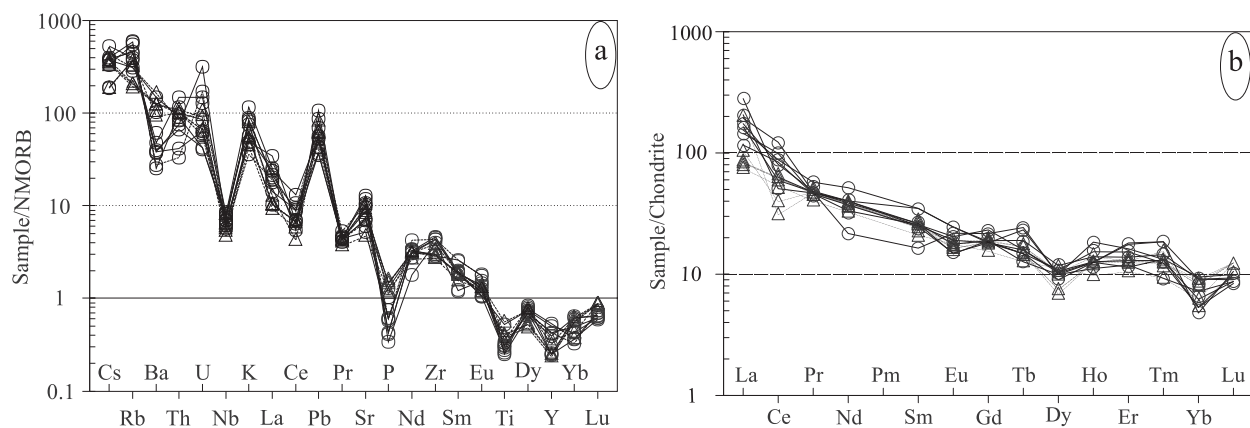


Fig. 4. a. NMORB-normalized trace element compositions. b. Chondrite-normalized REE patterns of the Lubin Zardeh volcanic samples (normalization factors from Sun and McDonough, 1989). Symbols as in Fig. 10d.

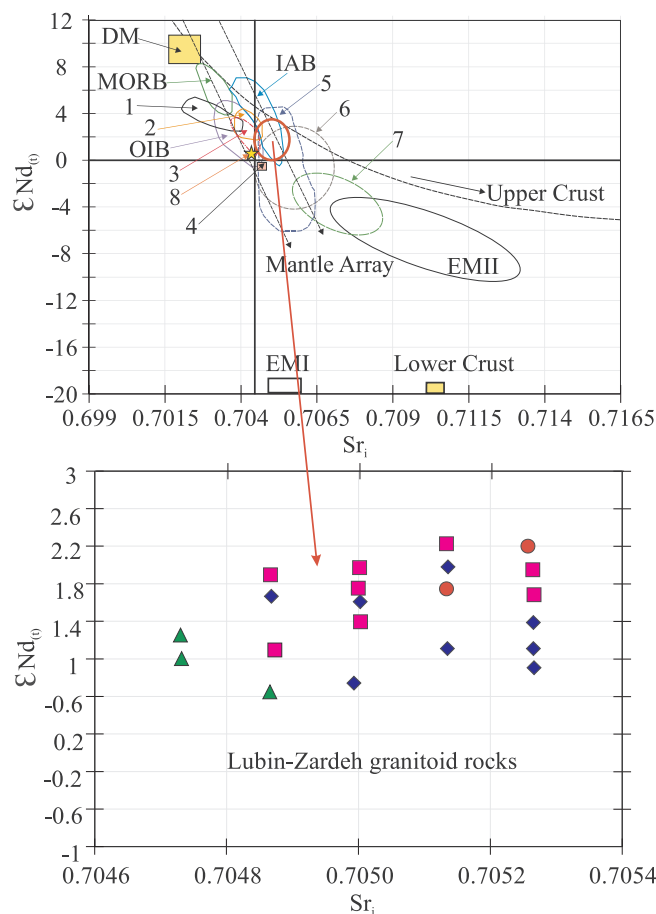


Fig. 5. Nd-Sr isotope compositions of the igneous host rock of Lubin-Zardeh deposit. Potassic and shoshonitic rocks from other sectors of the Tethyan orogenic belt (Tibet and Turkey) have been added for comparison. Data sources are as follows: 1 – Khalkhab granitoid; 2 – Oligocene plutons in the southeastern part of Urumieh-Dokhtar with porphyry copper mineralization; 3 – Shaviar Dagh pluton; 4 – Nd-Sr isotope compositions of the Sisdagi pluton from the Eastern Pontides; 5 – Tarom Sofla pluton; 6 – Alborz volcanic assemblage; 7 – Niyasar plutonic complex; 8 – Adakitic rocks in the Dexing area. DM: Depleted Mantle, EMI and EMII: enriched mantle; EMI and EMII represent two types of mantle end-members; IAB: Island Arc Basalts, MORB: Mid-Ocean Ridge Basalts, OIB: Ocean island basalts, SK: the SK line shows the average crustal growth curve of Stacey and Kramers (1975). Symbols as in Fig. 10d.

Sericite occurs as fine-grained (5–50 µm) crystals. Sericite occurs as fine grained (5–50 µm) crystals. Chlorite is green to brown in thin section and locally shows spheroidal (radial) textures. Illite and adularia are common alteration gangue minerals in volcaniclastic host rocks. Adularia is widespread and common (5 vol%) within the vein-veinlets. It occurs in quartz precious metal veins and veinlets as microscopic crystals. Plagioclase phenocrysts are replaced by adularia together, with quartz and clay.

7. Discussion

7.1. Evolution of ore-forming fluids and mineralization model

At the Lubin-Zardeh epithermal deposit, oxygen isotope and fluid inclusion data from mineralized ore veins suggest a model in which hydrothermal fluids of dominantly magmatic source ascended along extensional normal faults to higher levels, and mixed with circulating meteoric water. It was suggested that this fluid mixing may have been the dominant mechanism for gold-base-metal mineralization. Nevertheless, the occurrence of colloform/crustiform and plumose quartz along with fluid inclusion data indicate that boiling was another processes affecting hydrothermal fluids at Lubin-Zardeh (Zamanian et al., 2019).

Formation of epithermal deposits along the TMB indicate that this magmatic belt is a suitable location for epithermal mineralization in northwestern Iran. Previous work (Kouhestani et al., 2018, 2019; Mehrabi et al., 2016) suggests that a series of epithermal precious and base metal deposits and occurrences, i.e., Gulojeh, Aqkand, Aliabad-Khanchy, Chodarchay, Khalyfehlou, Chargar, Zajkan, Marshoun, Abbasabad, Zehabad, and Shah Ali Beiglou, were hosted in the volcanic, volcaniclastic and intrusive rocks in the TMB.

At deposit scale, (1) epithermal ore bodies in the TMB are of late Eocene age (Ghasemi Siani et al., 2015; Kouhestani et al., 2018; Mehrabi et al., 2016), mostly hosted by coeval or older volcanic-sub-volcanic rocks of the Karaj Formation. (2) Intersections between second or third order faults, fractures related to volcanic structures and breccia zones are the most favorable locations for mineralization. (3) Intensive and pervasive alteration zones are important indicators for epithermal ore bodies, especially vuggy quartz in HS (i.e., Chodarchay deposit) and quartz veins in IS deposits (i.e., Gulojeh, Aqkand, Aliabad-Khanchy, Khalyfehlou, Zajkan, Marshoun) that are more resistant to erosion. (4) Evidence of boiling is often observed in samples collected from surface outcrop in the epithermal deposits of the TMB. This is likely to represent the surface expression of a vein that has potential to host precious and base-metal mineralization. Furthermore, good evidence of boiling in surface samples indicates that the base of the boiling zone where precious and base-metal mineralization mostly likely occurred is

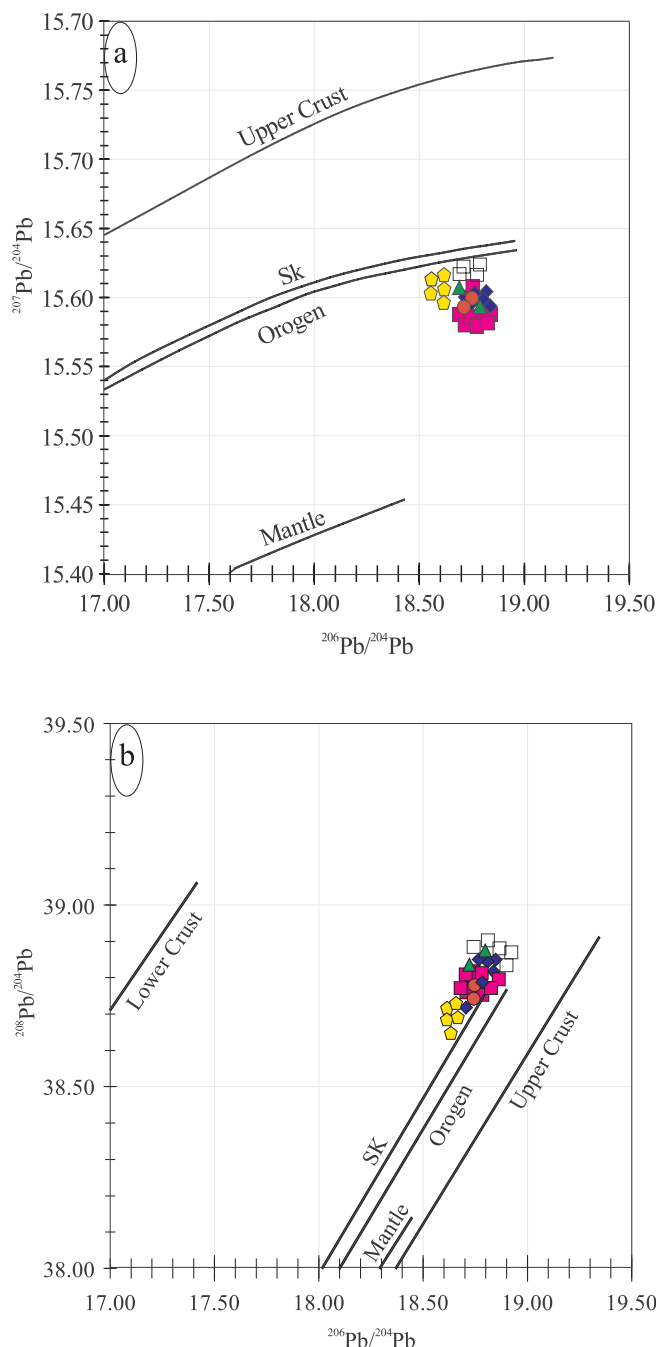


Fig. 6. a. Uranogenic diagram. b. Thorogenic diagram, comparing lead isotope compositions of the whole-rock samples of Lubin-Zardeh. Mantle, orogen, and upper crust evolution curves are from Doe and Zartman (1979) and the average crustal growth curve (SK line) is from Stacey and Kramers (1975). SK: the SK line shows the average crustal growth curve of Stacey and Kramers (1975). Symbols as in Fig. 10d.

beneath the present surface. Such an area might be given higher priority for drilling to explore the subsurface, even if metal grades in the surface samples are poor and sub-economic. (5) HS and IS epithermal deposits are commonly spatially and temporally associated with underlying and adjacent porphyry systems (Hedenquist and Arribas, 1998; Hedenquist et al., 2000; Li et al., 2016; Muntean and Einaudi, 2001; Pudack et al., 2009). Given the characteristics of the epithermal deposits in the TMB, it seems that this belt may host porphyry mineralization. The newly discovered Chodarchay deposit could be example of the transition from the deep porphyry mineralization

stage overprinted by the shallow HS epithermal stage in a porphyry–epithermal systems (Yasami et al., 2018; Yasami and Ghaderi, 2019). Nevertheless, more detailed work needs to be conducted in the future to constrain the genesis of the epithermal deposits and potential existence of porphyry deposits in this metallogenic belt. Detail geological, geochemical, and geophysical data may be able to identify drilling sites to explore for deeper porphyry-type deposits in the TMB.

7.2. Tectonic setting

The Lubin-Zardeh intrusive complex shows enrichment in LILE and LREE, relative to HREE and HFSE with negative anomalies in Ti, P, and Nb that display close similarities to those of the magmatic arc granites (Pearce et al., 1984). The high Ba/Zr (Ajaji et al., 1998) and Ba/Nb (Fitton et al., 1988) ratios are also indicative of subduction-related orogenic magmatism, because the high field strength elements (e.g., Zr, Nb, and Ti) are conservative and retained in the subducting slab, while the low field strength elements (e.g., Rb, Sr, K, Ba) are highly non-conservative and easily transported to the overlying zone of mantle melting (Briqueu et al., 1986; Kerrich and Wyman, 1997; Pearce, 1983). The averages of the Ba/Zr and Ba/Nb ratios in the studied intrusion are 3.1 and 44.7, respectively. Therefore, they are compatible with arc magmatism.

The Lubin-Zardeh intrusive complex and volcanic rocks samples are plotted on the various tectonic discrimination diagrams and most of the samples plot in the volcanic arc field (I-type) in the Ta vs. Yb diagram (Pearce et al., 1984; Fig. 9a). Furthermore, the presence of primary magnetite in the pyroxene and plagioclase indicates high oxygen fugacity in the parent magma (Nabatian et al., 2016; Sack et al., 1980). Moreover, Gorton and Schandl (2000) suggested that Th/Ta ratio is reliable for distinguishing between different tectonic settings, especially active continental margins from oceanic arc. Therefore, the Th/Ta ratios are consistent with an active continental margin setting (Fig. 9b). In addition, samples from the studied intrusion presented in a Th/Yb vs. La/Yb (Condie, 1989) diagram plot within the field of continental arc margin settings (Fig. 9c). Finally, rocks of the Lubin-Zardeh complex plot within the fields of continental arcs in the Zr/TiO₂ vs. Ce/P₂O₅ diagram (Müller and Groves, 1993, 1997; Fig. 9d) and the Hf-Rb/30-Ta*3 ternary (Harris et al., 1986) tectono-magmatic discrimination diagrams (Fig. 9e).

Thus in summary, the geochemical data and diagrams of the studied intrusion support an interpretation of a continental arc margin setting consistent with previous studies on the igneous rocks in the UDMA and AMB (e.g., Agard et al., 2005, 2011; Ahmadian et al., 2009; Alavi, 1994, 1991, 1996; Berberian and King, 1981; Haschke et al., 2010; Kananian et al., 2014; Sarjoughian et al., 2012). Also, voluminous magmatic rocks linearly distributed along the western margin of the Central Iranian and AMB within a number of obducted ophiolites from the collisional suture zones, are more geological evidence of the presence of an arc in Iran. It seems that the Eocene magmatic event may have been a consequence of complex processes involving the subduction of the Neotethys oceanic crust underneath central Iran structural zone.

7.3. Magma Genesis

Here we discuss the different possibilities for generating the Lubin-Zardeh intrusive complex, in AMB, from these various perspectives. Although Lubin-Zardeh intrusive complex shows typical adakitic compositional features (e.g., high Sr/Y and La/Yb), they are high in K₂O (ave: 4.7 wt%), which is much higher than adakites from slab melting (Defant and Drummond, 1990), and is dissimilar to those of adakites derived from slab melting. They also have higher Th (ave.: 9.7 ppm) and Th/Ce (ave.: 0.2) than subducted slab-derived adakites (Wang et al., 2006a). Fig. 10a shows that high Ba/Nb ratios tend to be negatively correlated with Nb concentrations. If slab melts were directly



(caption on next page)

Fig.7. a. Field photographs demonstrating intrusive rocks, quartz-sulfide vein and the Lubin-Zardeh deposit in the study area (looking northward). b. Photograph of a mineralized vein (light-colored minerals are quartz, sericite, clay minerals and dark ones are sulfide minerals such as chalcopyrite, pyrite, chalcocite). c. General view of the quartz bearing copper-gold deposit zones. d. Hand specimen of quartz monzonite. e. Hand specimen of crystal tuffs. f. Hand specimen of hydrothermal breccia. g. Silicified tuff cut by crystalline quartz veinlets and subparallel sheeted stage 2 quartz veinlets crosscutting stage 1 quartz vein. Afs: alkali feldspar, Amp: amphibole, Ccp: chalcopyrite, Gn: galena, Pl: plagioclase, Qz: quartz, Ser: sericite, Sp: sphalerite.

involved in the petrogenesis of the studied rocks, a positive correlation between Ba/Nb and Nb should be observed, as adakitic magmas are thought to transport Ba and Nb into the mantle wedge (Bourdon et al., 2002; Kesson and Ringwood, 1989); however, it is unlikely that the studied intrusions have been derived by partial melting of a subducted oceanic slab. Also, they are characterized by bulk Earth-like Nd-Sr isotope compositions $\epsilon\text{Nd}_{(t)} = +0.39$ to $+2.1$ and initial $^{87}\text{Sr}/^{86}\text{Sr} = 0.7047$ – 0.7051 , which are inconsistent with slab-derived adakites. In addition, the age of the subducting slab becomes critical. The Arabian plate at 50 Ma is clearly too old and cold to form slab-derived adakites. Hence we conclude that the studied intrusions were unlikely to have been produced by partial melting of subducted oceanic crust.

Adakitic characteristics can be derived by Assimilation and Fractional Crystallization (AFC) processes. The following evidence indicates that these basalts did not result from AFC processes: (1) Coexisting mafic rocks within the Lubin-Zardeh intrusive complex occur in very small volumes, and it is unlikely that fractionation of such small volumes of mafic magmas could be responsible for the large volumes of granitoid rocks (see Xu et al., 2002); (2) Approximately constant Nd/Sr and high Sr concentrations of the studied intrusion suggest that the mafic magma could not evolve to form magma with adakitic compositional features by fractional crystallization of plagioclase (see Wang et al., 2004a); (3) Their Sr/Y and La/Yb ratios have no obvious correlations with MgO and SiO₂, suggesting that high Sr/Y and La/Yb ratios were inherited from a source region rather than produced by magma differentiation (see Zhao and Zhou, 2008); (4) The low Rb/Sr ratios (ave.: 0.3) rule out an origin from a mafic magma by extensive fractional crystallization (see Mirnejad et al., 2013); and (5) The Dy/Yb vs. Dy diagrams (see Gao et al., 2007; Fig. 10b) indicate that the studied intrusions has not undergone fractional crystallization and reflects an end-member partial melting model. Therefore, crustal AFC processes involving basaltic magma cannot produce the Lubin-Zardeh intrusive complex.

The relatively high SiO₂ (56–74 wt%) contents of the studied intrusion phases indicate that they could not be directly generated by partial melting of mantle peridotite, because low degree partial melting of mantle peridotite cannot yield acidic magmas (Green, 1980; Jahn and Zhang, 1984; Wang et al., 2006b). Anhydrous lherzolite melting experiments (Baker et al., 1995) also shows that the composition of low percentage partial melts will not be more silicic than andesites, ~55 wt % SiO₂ at 2% melt fractions. Therefore, the studied intrusion could not have been directly derived from the partial melting of mantle peridotites (Wang et al., 2004b). In addition, partial melting of mantle peridotite cannot produce volumetrically significant felsic rocks.

Partial melting of intermediate-mafic rocks in the lower crust, heated by underplating mantle mafic magmas, is another mechanism that may yield adakitic magma (Atherton and Petford, 1993; Gromet and Silver, 1987; Petford and Atherton, 1996). Adakitic magmas formed directly from the lower crust generally have relatively low MgO contents or Mg# (Rapp et al., 1991, 1999; Rapp and Watson, 1995; Sen and Dunn, 1994; Skjerlie and Patiño Douce, 2002; Springer and Seck, 1997; Winther, 1996). They also have low Ni and V contents, high initial $^{87}\text{Sr}/^{86}\text{Sr}$ ratios (0.7048–0.705), and low ϵNd values (0.39–2.1) similar to those of crustal rocks (Wang et al., 2004a); these characteristics indicate that the Lubin-Zardeh intrusive complex is not derived by lower crust melting alone. Also, their Mg# values are higher than that of experimental melts of metabasalts and eclogites at pressures of 1.0–4.0 GPa (cf. Atherton and Petford, 1993; Green, 1994) implicating

that they did not simply originate from partial melting of a thickened lower crust. In the Rb/Sr versus La/Ce (Fig. 10c) diagrams (Hofmann et al., 1986; Hou et al., 2004), the compositions of the rocks from the Lubin-Zardeh intrusive complex plot between continental crust-derived melt and MORB/slack-derived melts, with closer affinity to a crustal source.

Correspondingly, the discrimination ratios during the fractionation of magma, including Nb/Ta and Zr/Nb are moderate values in this intrusive complex (Ave. 25 and 16.0, respectively), compared to magma derived from the enriched mantle (Nb/Ta: 17 and Zr/Nb: 6; Sun and McDonough, 1989), and magma derived from the lower crustal source (Nb/Ta: 11 and Zr/Nb: 25; Weaver and Tarney, 1984). Therefore, it seems that they have a hybrid genesis. Also, higher $^{87}\text{Sr}/^{86}\text{Sr}$ and lower $^{143}\text{Nd}/^{144}\text{Nd}$ relative to adakites from mantle, and lower $^{87}\text{Sr}/^{86}\text{Sr}$ and higher $^{143}\text{Nd}/^{144}\text{Nd}$ relative to adakites from lower crust melting suggest that the Lubin-Zardeh intrusions originated from partial melting of the delaminated lower continental crust (LCC), followed by interaction with the mantle peridotites.

In terms of geochemical and isotopic compositions, the Dexing adakitic porphyries (South China) exhibit relatively high Al₂O₃ (14.50–17.50 wt%), Sr (442–2301 ppm), MgO (1.80–5.00 wt%), Cr (30–120 ppm), and Ni (12–36 ppm) contents, with high Sr/Y (34–254), and initial $^{87}\text{Sr}/^{86}\text{Sr}$ ratios (0.7044–0.7047) and low Yb (0.28–1.40 ppm) contents, and $\epsilon\text{Nd}_{(t)}$ (−1.14–1.8) (Wang et al., 2006b), are similar to the Lubin-Zardeh intrusive complex (demonstrated above). This suggests it was derived by melting of delaminated thickened lower continental crust, followed by subsequent interactions with peridotite during upward emplacement.

Rapp et al. (2002) suggested that the origins of high K₂O contents is likely related to high-pressure (more than 1.0 GPa) melting. Therefore, the origins of relatively high K₂O contents in the studied complex is probably related to high pressure partial melting of delaminated lower crust. The melt will pass through the metasomatized mantle, as it rises towards the surface, elevating their MgO, Mg#, Ni, and Cr values, and decreasing Al₂O₃, Na₂O, and SiO₂ contents by the interaction between lithospheric mantle melt. Therefore, the initial magmas experienced different degrees of interaction with the mantle during ascent (e.g., Atherton and Petford, 1993; Gao et al., 2004; Kepezhinskas et al., 1995; Liu et al., 2010; Rapp et al., 1999; Xu et al., 2002; Yogodzinski et al., 1995; Zhao and Zhou, 2008). In the Lubin-Zardeh, intrusive complex is mostly potassic with distinctly higher K₂O contents (ave.: 4.9 wt%) and K₂O/Na₂O (ave.: 1.11). The differences in K₂O contents and K₂O/Na₂O can be explained by the presence of amphibole in the various sources. This is because amphibole is the main K-bearing mineral, having much higher K₂O than garnet and clinopyroxene in residual phases during high-pressure melting of metabasaltic rocks (e.g., Liu et al., 2010; Rapp and Watson, 1995; Sen and Dunn, 1994). The rocks are characterized by enrichment of LILE and depletion of HFSE, strongly fractionated REE pattern (ave.: La_n/Yb_n: 14.31), concave-upward REE patterns, negative anomalies in Nb and Ti, coupled with positive anomalies in Sr and do not contain significant Eu anomalies. The low HREE and Y contents and the high Sr/Y and La/Yb ratios can be attributed to the presence of garnet and hornblende in the residue resulting from partial melting of their source (Atherton and Petford, 1993; Defant and Drummond, 1990). Because garnet has high partition coefficients of HREE and Y relative to LREE and Sr (Rollinson, 1993), these rocks have low Yb_n and highly variable La_n/Yb_n ratios, suggesting that the source was a hydrous amphibole eclogite or eclogite (Zhou et al., 2006). Lack of a negative Eu anomaly indicates a lack of plagioclase fractionation from primitive

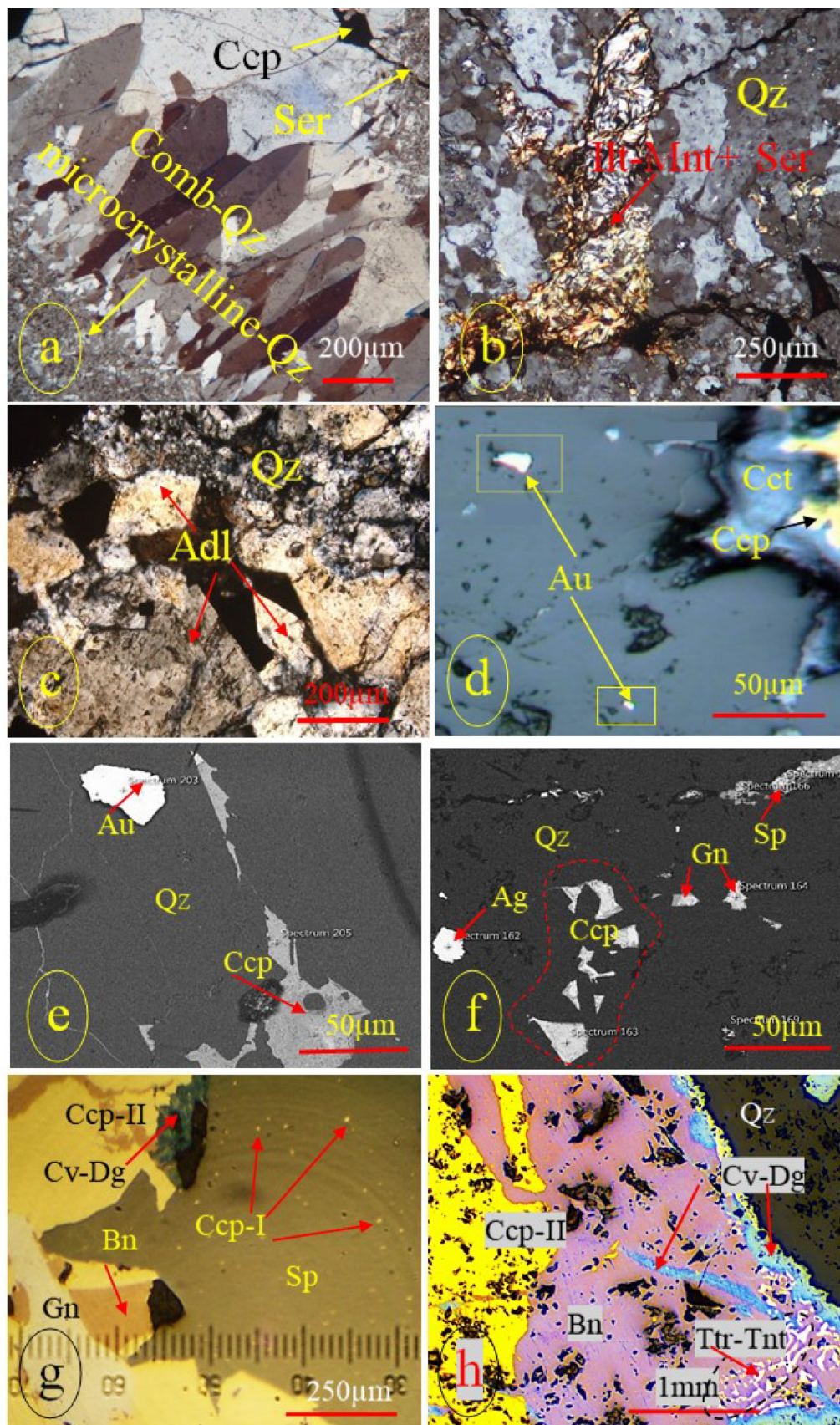
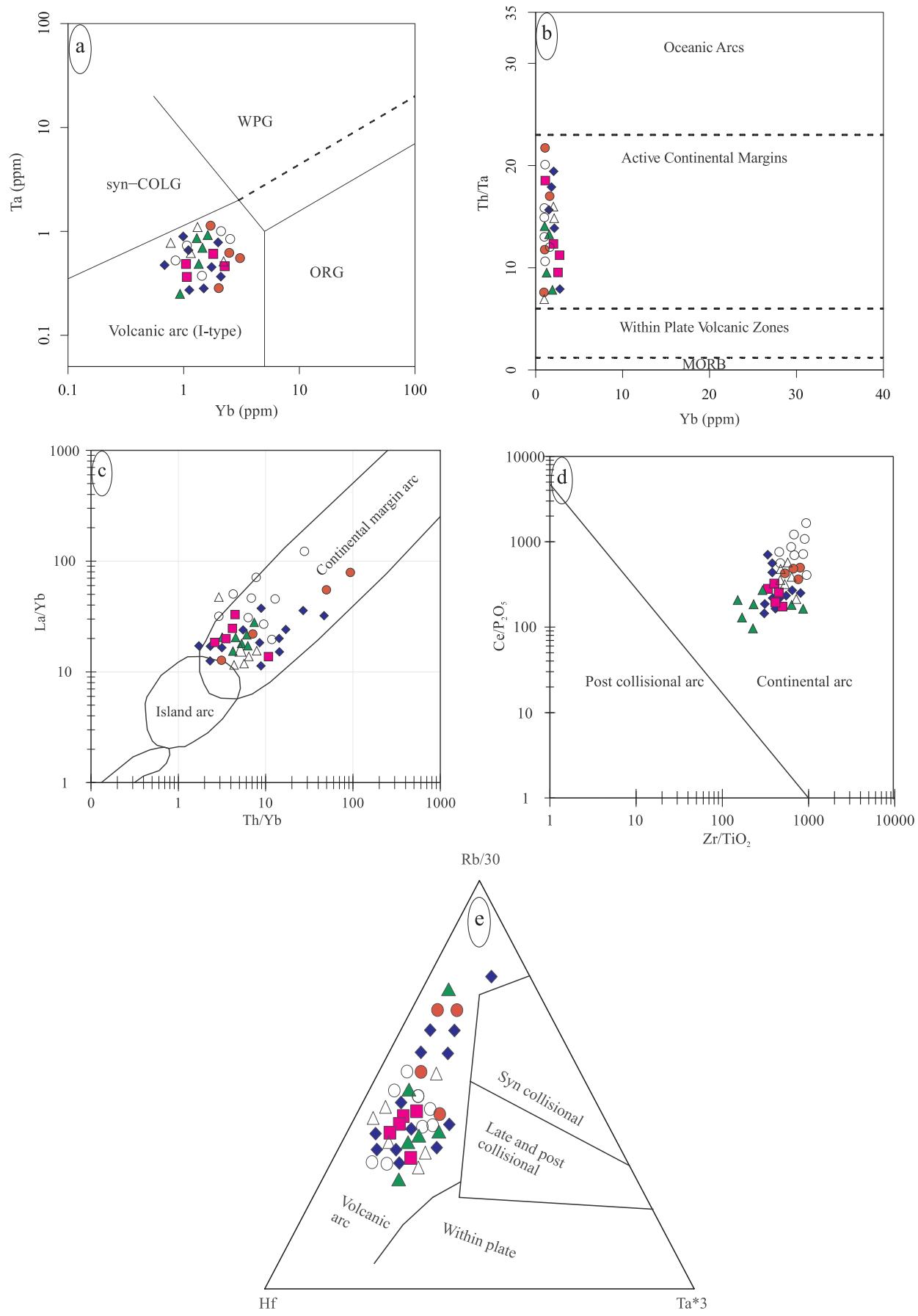


Fig.8. Photomicrographs (transmitted polarized-light, XPL) of wall-rock alteration types at Lubin-Zardeh deposit. a. Sericitic and silicic alteration zone, quartz occasionally showing micro-crystalline, chalcedony and plumose quartz texture. b. Argillic alteration zone (clay minerals like illite and montmorillonite) of the tuff breccia wall rock. c. Euhedral adularia and quartz as vein fillings. d. Image of native gold particle in silica gangue that is the paragenesis with chalcopyrite. e. SEM image from polished section of a sample native gold particle associated with quartz gangue. f. SEM image of native silver in quartz-veins. g. Fine grained inclusions of chalcopyrite are present in the sphalerite. h. Chalcopyrite is replaced by bornite along cleavage and fractures, anhedral crystals of tetrahedrit-tennantite is enclosed within bornite is replaced covellite – digenite in its crystal boundaries. Au: native gold, Ag: native silver, Bn: bornite, Ccp: chalcopyrite, Ccp-I: first generation chalcopyrite, Ccp-II: second generation chalcopyrite, Cct: chalcocite, Cv: covellite, Dg: digenite, Gn: galena, Ilt: illite, Mnt: montmorillonite, Pl: plagioclase, Py: pyrite, Qz: quartz, Ser: sericite, Sp: sphalerite, Ttr: tetrahedrite, Tnt: tennantite. Abbreviations according to Whitney and Evans (2010).



(caption on next page)

Fig.9. a. Geotectonic trace-element discrimination diagrams of Pearce et al. (1984). b. Geotectonic trace-element discrimination diagrams of Gorton and Schandl (2000) and c. Geotectonic trace-element discrimination diagrams of Condie (1989). d and e. Distribution of the samples in the geotectonic trace-element discrimination diagrams of Müller and Groves (1997) and Harris et al. (1986). MORB: Mid-Oceanic Ridge Basalts, ORG: Ocean Ridge Granites, Syn-COLG: syn-collision Granites, WPG: within plate Granites. Symbols as in Fig. 10d.

magmas, suppression of plagioclase fractionation due to high magmatic water contents, and (or) high magmatic oxidation state, such that most of the Eu is present in the trivalent state and is not partitioned into fractionating plagioclase (Frey et al., 1978; Hanson 1980; Richards et al., 2012). Furthermore, amongst the HREE, Yb, and Lu have the highest garnet-melt partition coefficients, whereas Dy and Ho have the highest hornblende-melt partition coefficients (Sisson, 1994). When garnet is the main residual phase, HREE will show strongly fractionated patterns with $Y/Yb > 10$. In contrast, when hornblende is the main residual phase, HREE will show flat patterns with $Y/Yb \approx 10$ (Ge et al., 2002). The Y/Yb ratio of the studied intrusions is 8.67–12.24 with the concavity of the middle REE and moderate low K/Rb (ave.: 246)

indicating that residual hornblende likely existed in the source regions (Arth and Hanson, 1975; Gromet and Silver, 1987; Wang et al., 2004a).

High Sr contents and the absence of significant Eu anomalies and high Sr/Ba (ave.: 1.6) preclude significant residual plagioclase in the source (Arth and Hanson, 1975; Barnes et al., 1996; Hou et al., 2004; Mo et al., 2007). The Nb and Ti negative anomalies are typical of all types of calc-alkaline magmas and they may be explained by residual hornblende and (or) Fe-Ti oxides (rutile and ilmenite) in the source of the parental magmas (Hou et al., 2004; Tatsumi, 1986), because Nb tends to be hosted in amphibole, being at equilibrium with 60–70 wt% SiO_2 melt during partial melting (Pearce and Norry, 1979). Titanium would be hosted in rutile under hydrous mantle conditions (Tatsumi,

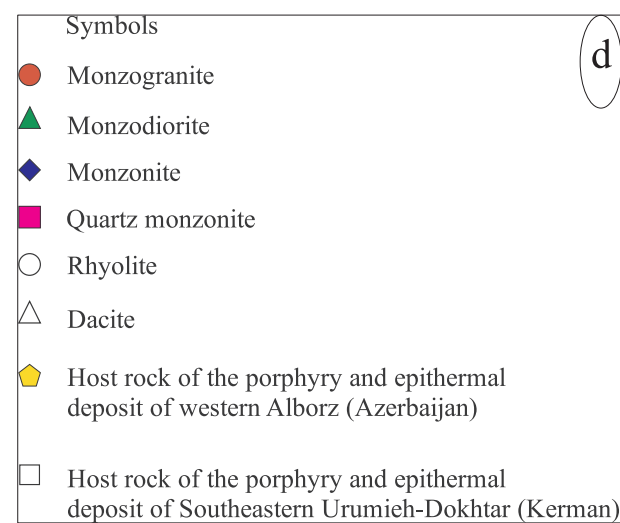
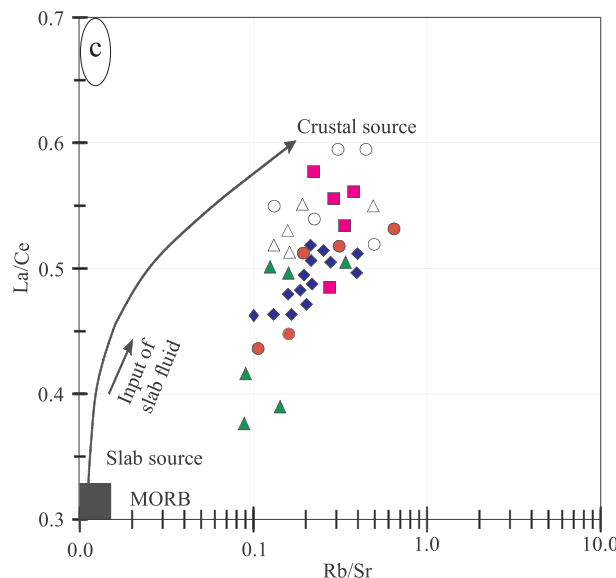
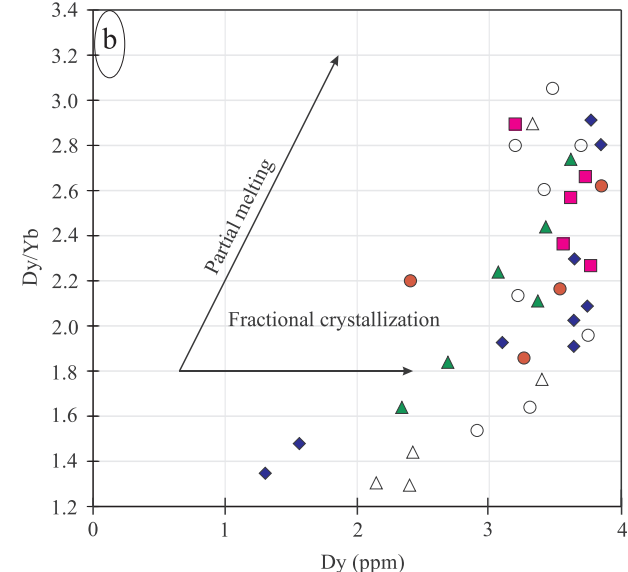
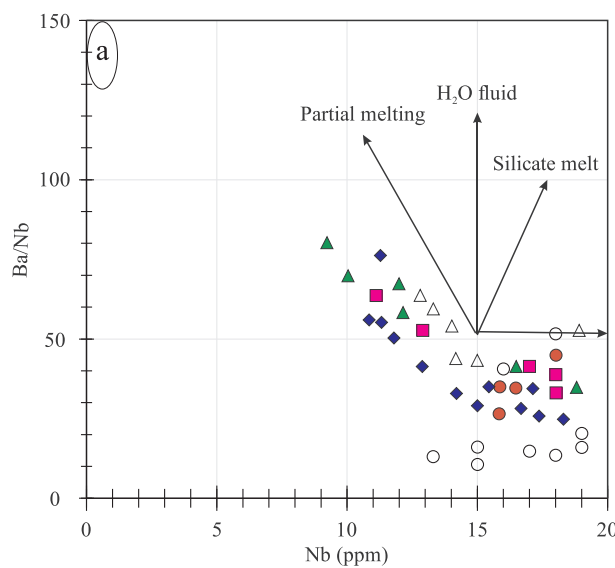


Fig.10. a. Nb versus Ba/Nb diagram (Bourdon et al., 2002) with sample distribution which demonstrates a trend consistent with the partial melting process.b. Dy/Yb versus Dy diagrams illustrating trends of fractional crystallization and versus partial melting processes. c. Rb/Sr versus La/Ce diagrams (Hofmann et al., 1986) which illustrates the distribution of samples in the Lubin-Zardeh deposit. d. Symbols of plutonic and volcanic rocks. MORB: Mid-Oceanic Ridge Basalts, FC: Fractional Crystallization.

1986; Zhou et al., 2006). Some researchers (e.g., Gust et al., 1997; Martin, 1999; Woodhead et al., 1993) suggested that their high Sr and low Nb, Ta, and Ti contents are due to the absence of plagioclase and presence of Fe–Ti oxides in the residue in the source area of the parental magmas. Niobium and Ta contents may also be viewed as resulting from previous depletion events in the mantle source rocks and (or) the fractionation of Ti-bearing phases, such as titanite (Arjmandzadeh et al., 2011). Martin (1999) believed that the strong Nb and Ta and weak Ti negative anomalies, and absent Zr and Hf depletions, indicate residual rutile in the source, with small to moderate degrees of partial melting of eclogitic basalts at higher pressure (Gao et al., 2007; Rapp et al., 1991). These characteristics suggest that the source has residual garnet, amphibole, and possibly rutile, and thus is most likely garnet-bearing amphibole and (or) amphibole-bearing eclogite. It supports a geochemical batch melting modeling that indicates low- to medium-degree partial melting (5–10%) of a garnet-bearing (up to 5%) basaltic amphibolite source, and lack of plagioclase as a residual component in the source for the Lubin-Zardeh intrusive complex (Rahmani et al., 2018).

Experimental petrology and phase equilibria research (Huang and Wyllie, 1986) indicate that when the pressure is 1 GPa, the liquidus mineral of the andesitic magma system is plagioclase ± pyroxene; when > 1 GPa, it is pyroxene ± garnet ± amphibole. In cases where the buried depth is more than 45 km, continental crust will be transformed into eclogite (Lai et al., 2003; Yardley and Valley, 1997). Other experimental studies (e.g., Rapp and Watson, 1995; Rapp et al., 1999, 2002, 2003) have also shown that the adakitic liquids can be produced by melting of mafic materials at pressures equivalent to crustal thicknesses of > 40–50 km (i.e., > 1.2 GPa), when the residual phases include garnet, garnet-amphibolite, but little or no plagioclase, most probably under eclogite facies conditions (Wang et al., 2006b). In summary, we conclude that source materials in the lower portions of thickened crust in the Lubin-Zardeh intrusive complex consisted of amphibole-bearing eclogitic and garnet-bearing amphibolitic materials with relatively high K₂O.

Wedepohl (1995) believed that in some areas with their larger thicknesses mafic granulite have transformed into eclogites with a density higher than that of lherzolite that sinks into the mantle been detached from the lower crust. Eclogite is formed through high- to ultrahigh-pressure metamorphism of basaltic rocks and has a density that is higher than peridotite by 0.2–0.4 g cm⁻³ (Rudnick and Fountain, 1995). Because of this density contrast, mafic lower continental crust (together with the underlying lithospheric mantle) can be recycled into the mantle and leads to delamination (Ducea and Saleeby, 1998; Kay and Kay, 1993; Wang et al., 2004b; Xu et al., 2002), when granulite is transformed into eclogite during crustal thickening (Gao et al., 2004; Jull and Kelemen, 2001; Kay and Kay, 1991; Wang et al., 2006b). Foundering of a dense, unstable lithospheric root into the mantle through delamination caused the replacement of eclogite by buoyant, warm asthenosphere that underwent decompressional melting to produce basaltic liquids (Dilek and Altunkaynak, 2007). When the eclogitic material was delaminated, the temperatures along the contacts between hot mantle and the eclogitic materials would have been high enough to trigger dehydration melting of amphibole-bearing eclogites at pressures > 1.2 GPa (Rapp et al., 1991; Rapp and Watson, 1995; Wolf and Wyllie, 1994), which is consistent with > 40 km thick Eocene Alborz crust, forming adakitic magmas (e.g., Rapp et al., 1999, 2002). However, the present-day crustal thickness in the Lubin-Zardeh area in Alborz is about 50 km, according to a geophysical survey by Sodoudi et al. (2009). Their data imply that the Eocene continental crust in the Lubin-Zardeh area in Alborz was thicker (> 40 km) than the present crust, and the continental crust, therefore, has most likely undergone a thinning process. Also, Quaternary sedimentary rocks are still preserved in the Alborz area, suggesting that the upper crust in this area has not undergone extensive erosion since the Eocene.

We suggest that the slower convergence rate caused crustal

thickening (e.g., Shellnutt et al., 2014) and that caused increasing crustal thickness caused, which resulted in delamination of the lower crust and emplacement of the hot asthenosphere that generated the adakitic magmatism (Jamali and Mehrabi, 2015). This delaminated lower crust hypothesis generally involves continent–continent collision and (or) intracontinental subduction, crustal thickening, and then delamination (see Wang et al., 2007); following delamination or foundering, the lower crust would have been heated by the surrounding mantle. Delamination of sub-continental mantle lithosphere with ingress of asthenospheric melts into the lower crust can cause partial melting of the metasomatized lithosphere (Brown, 2010; Richards, 2009). Potential energy that is released drives the process, as hot, low-density asthenospheric mantle replaces cold, dense lithosphere, accompanied by lithospheric thinning and increased magma production (Bird, 1979; Kay and Kay, 1991, 1993). Therefore, we conclude that delamination could also explain the thinning of the Eocene crust in this part of Alborz, as a consequence of sinking of eclogitic material from the base of the lithosphere into the underlying mantle. It follows that underplating of mafic magmas related to the Neo-Tethyan subduction and subsequent Arabian–Iranian plate collision was a result of lithospheric delamination. This is supported by Aghazadeh et al. (2011), Asiabana and Foden (2012), Castro et al. (2013), Hatzfeld and Molnar (2010), Moayyed (2001), Nabatian et al. (2014, 2016), Shomali et al. (2011) who proposed lithospheric delamination underneath the Zagros collision zone in southwest Iran. Therefore, lithospheric thinning and possible delamination of thickened continental crust was likely responsible for the advective heat transfer that caused fusion of those metasomatized crustal segments. Subsequent reaction with the invading mantle during buoyant ascent was responsible for the petrogenesis of the Lubin-Zardeh adakitic rocks.

In Fig. 6a, b the intrusive rocks samples plot on the Pb isotope orogen curve of Doe and Zartman (1979) and, as could be expected, at an approximately zero age. “Orogen” as defined by Doe and Zartman (1979) encompasses a number of geotectonic settings in which the proportion of mantle and crustal components incorporated may vary considerably. Lead from a primitive, intra-oceanic island arc will tend to plot closer to the mantle curve, whereas lead from a continental margin setting plots closer to the orogen curve (Doe and Zartman, 1979).

Combining the Pb-isotope data with petrogenetic considerations suggests derivation of the ore-hosting granitoids from a mixed reservoir with slightly radiogenic Pb values, such as a hybridized lower continental crustal source.

The Pb-isotope composition of the ore-hosting granitoids exhibit relatively homogenous, radiogenic Pb-isotope values with orogenic character. These granitoids were formed and emplaced in a thickened arc crust during an overall compressional regime.

The uniformity and orogenic character of the Pb-isotope data for the ore-hosting granitoids in the Tarom suggest their derivation from a mixed and relatively homogeneous isotopic reservoir, with U/Pb ratios lower than those of the average crust, such as hybridized lower continental crust.

8. Conclusions

1. The Lubin-Zardeh deposit is the result of late Eocene-Oligocene fault-controlled hydrothermal activity related to the I-type quartz monzonite intrusion emplaced in a continental arc environment.
2. The geochemical features, such as enrichment in LILE and LREE and negative Nb, Ta and Ti anomalies together with the initial ratio of ⁸⁷Sr/⁸⁶Sr and Pb isotopes, suggest a chemically enriched lithospheric mantle source. Furthermore, the source of magma has been enriched in LILEs over HFSEs by the possible role of residual rutile in the source material or metasomatic activity of fluids derived from the subducted slab and sediments, which carry crustal elemental and isotopic signatures. In this case, the source materials have been

- modified by the recycled product of terrigenous sediments from an earlier subduction (Beccaluva et al., 2004; Zindler and Hart, 1986).
3. Low values of TiO_2 in the studied samples are also related to the residual Ti phases (e.g., titanite and rutile) in the hydrated mantle source (Foley and Wheller, 1990). The chondrite-normalized rare earth element patterns for the selected samples from the pluton show slight enrichment in MREE, which can indicate the presence of amphibole as another hydrous mineral in the source mantle. Moreover, the high contents of Rb and Ba may suggest phlogopite as one of the metasomatic products in the upper mantle peridotite (Müller and Groves, 2000). In this case, the resulting melt would be more enriched in K and Ba compared to Rb, as one can see in the host rocks pluton.
 4. Therefore, the parental magma of the Lubin-Zardeh pluton is likely derived from partial melting of a phlogopite-bearing, amphibole-rich mantle source. In the Tarom area, partial melting of the metasomatized mantle might have resulted from the latest Eocene lithospheric thinning and hot asthenospheric upwelling during the final stage of Neotethyan subduction through slab rollback or shortly after the cessation of arc magmatism.
 5. Geochemical features and high water content can be inferred from hornblende in igneous host rocks by the wide extent of hydrothermal alteration, suggesting a more adakitic nature and, which favor epithermal and porphyry mineralization.
 6. Based on textural evidence (coarse amphibole crystals), geochemical data (major, trace and Rare-Earth Elements) and isotopic contents of lead, strontium-neodymium, it is suggested that these rocks are similar to the host rocks of porphyry and epithermal deposits in the Urumieh-Dokhtar from the viewpoint of geochemical and isotopic compositions (Rezaei-Kahkhaei et al., 2011; Shafiei et al., 2009), West Alborz-Azerbaijan (Arasbaran; Aghazadeh et al., 2013) and Eastern Pontides Arc (Turkey; Karsli et al., 2012) porphyry and epithermal deposits.

Declaration of Competing Interest

The authors declare that they have no known competing financial interests or personal relationships that could have appeared to influence the work reported in this paper.

Acknowledgements

This research was financially supported by the Lorestan University and the Geological Survey of Iran. M.R. Jannessary (Deputy Director for Mineral Exploration, Geological Survey of Iran) is thanked for providing field logistics. Also R. Sepehrirad is thanked for preparing the digital illustrations. G. Nabatian, S. Sehhat and R. Zenoozi are thanked for help in radiogenic isotope and mineralogical studies. We also appreciated Prof. Pirajno, Prof. Lentz and anonymous Reviewers for their constructive suggestions on the manuscript.

Appendix A. Supplementary data

Supplementary data to this article can be found online at <https://doi.org/10.1016/j.oregeorev.2020.103496>.

References

- Agard, P., Omrani, J., Jolivet, L., Mouthereau, F., 2005. Convergence history across Zagros (Iran): constraints from collisional and earlier deformation. *Int. J. Earth Sci.* 94, 401–419.
- Agard, P., Omrani, J., Jolivet, L., Whitechurch, H., Vrielynck, B., Spakman, W., Monié, P., Meyer, B., Wortel, R., 2011. Zagros orogeny: a subduction-dominated process. *Geol. Mag.* 148, 692–725.
- Aghazadeh, M., Castro, A., Badrzadeh, Z., 2013. Late Eocene-Oligocene post-collisional monzonitic intrusions from the Alborz magmatic belt, NW Iran. An example of monzonite magma generation from a metasomatized mantle source. *Lithos* 03051, 1–19.
- Aghazadeh, M., Castro, A., Badrzadeh, Z., Vogt, K., 2011. Post-collisional polycyclic plutonism from the Zagros hinterland: the Shaivar Dagh plutonic complex, Alborz belt, Iran. *Geol. Mag.* 148, 980–1008.
- Aguillon-Robles, A., Caimus, T., Bellon, H., Maury, R.C., Cotton, J., Bourgois, J., Michaud, F., 2001. Late Miocene adakites and Nb-enriched basalts from Vizcaino Peninsula, Mexico: indicators of East Pacific Rise subduction below southern Baja California. *Geology* 29, 531–534.
- Ahmadian, J., Haschke, M., McDonald, I., Regelous, M., Ghorbani, M., Emami, M., Murata, M., 2009. High magmatic flux during Alpine-Himalayan collision: Constraints from the Kal-e-Kafi complex, central Iran. *Geol. Soc. Am. Bull.* 121, 857–868.
- Ajaji, T., Weis, D., Giret, A., Bouabdellah, M., 1998. Coeval potassic and sodic calc-alkaline series in the postcollisional Hercynian Tancherchi intrusive complex, northeastern Morocco: geochemical, isotopic and geochronological evidence. *Lithos* 45, 371–393.
- Alavi, M., 1991. Tectonic map of the Middle East (scale 1:5,000,000). *Geol. Surv., Iran.*
- Alavi, M., 1994. Tectonic of the Zagros orogenic belt of Iran: new data and interpretations. *Tectonophysics* 229, 211–238.
- Alavi, M., 1996. Tectonostratigraphic synthesis and structural style of the Alborz mountain system in northern Iran. *J. Geodyn.* 21, 1–33.
- Amini, B., Amini, M.R., Stocklin, J., Hirayama, K., 2001. Geological map of Tarom, sheet no.5763, 1: 100,000 scale. Geological Survey of Iran.
- Arjmandzadeh, R., Karimpour, M.H., Mazaheri, S.A., Santos, J.F., Medina, J.M., Homama, S.M., 2011. Sr-Nd isotope geochemistry and petrogenesis of the Chah-Shaljami granitoids (Lut Block, Eastern Iran). *J. Asian Earth Sci.* 41, 283–296.
- Arth, J.G., Hanson, G.N., 1975. Geochemistry and origin of the early Precambrian crust of northeastern Minnesota. *Geochim. Cosmochim. Acta* 39, 325–362.
- Asadi, S., Moore, F., Zaravandi, A., 2014. Discriminating productive and barren porphyry copper deposits in the southeastern part of the central Iranian volcano-plutonic belt, Kerman region, Iran: a review. *Earth Sci. Rev.* 138, 25–46.
- Asiabanza, A., Foden, J., 2012. Post Collisional transition from an extensional volcano-sedimentary basin to a continental arc in the Alborz Ranges, N-Iran. *Lithos*. 148, 98–111.
- Atherton, M.P., Petford, N., 1993. Generation of sodium-rich magmas from newly underplated basaltic crust. *Nature* 362, 144–146.
- Ayati, F., Yavuz, F., Asadi, H., Richards, J.P., Jourdane, F., 2013. Petrology and geochemistry of calc-alkaline volcanic and subvolcanic rocks, Dalli porphyry copper-gold deposit, Markazi Province, Iran. *Int. Geol. Rev.* 55, 158–184.
- Azizi, H., Jahangiri, A., 2008. Cretaceous subduction-related volcanism in the northern Sanandaj-Sirjan Zone, Iran. *J. Geodyn.* 45, 178–190.
- Azizi, H., Moinevaziri, H., 2009. Review of the tectonic setting of Cretaceous to Quaternary volcanism in northwestern Iran. *J. Geodyn.* 47, 167–179.
- Azizi, H., Tanaka, T., Asahara, Y., Chung, S.L., Zarrinkoub, M.H., 2011. Discrimination of the age and tectonic setting for magmatic rocks along the Zagros thrust zone, northwest Iran, using the zircon U-Pb age and Sr-Nd isotopes. *J. Geodyn.* 52, 304–320.
- Baker, M.B., Hischmann, M.M., Ghiorso, M.S., Stolper, E.M., 1995. Compositions of near-solidus predictive melts from experiments and thermodynamic calculations. *Nature* 375, 308–311.
- Barnes, C.G., Petersen, S.W., Kistler, R.W., Murray, R., Kay, M.A., 1996. Source and tectonic implications of tonalite-trondhjemite magmatism in the Klamath Mountain. *Contrib. Miner. Petrol.* 123, 40–60.
- Barton Jr., P.B., Bethke, P.M., 1987. Chalcopyrite disease in sphalerite: pathology and epidemiology. *Am. Mineral.* 72, 451–467.
- Beccaluva, L., Bianchini, G., Bonadiman, C., Siena, F., Vaccaro, C., 2004. Coexisting anorogenic and subduction-related metasomatism in the mantle xenoliths from the Betic Cordillera (southern Spain). *Lithos* 75, 67–87.
- Bente, K., Doering, Th., 1993. Solid-state diffusion in sphalerites: an experimental verification of the “chalcopyrite disease”. *Eur. J. Mineral.* 5, 465–478.
- Berberian, F., Muir, I.D., Pankhurst, R.J., Berberian, M., 1982. Late Cretaceous and early Miocene Andean-type plutonic activity in northern Makran and Central Iran. *J. Geol. Soc. London* 139, 605–614.
- Berberian, M., King, G.C.P., 1981. Towards a paleogeography and tectonic evolution of Iran. *Can. J. Earth Sci.* 18, 210–265.
- Bird, P., 1979. Continental delamination and the Colorado Plateau. *J. Geophys. Res.* 84, 7561–7571.
- Bonev, I.K., Radulova, A., 1994. Chalcopyrite and sphalerite “diseases”: Crystal growth b-solid state diffusion. *IMA 16th General Meeting, Pisa-1994, Italy. Abstracts*, 50.
- Bortnikov, N.S., Genkin, A.D., Dobrovolskaya, M.G., Muravitskaya, G.N., Filimonova, A.A., 1991. The nature of chalcopyrite inclusion in sphalerite: exsolution, coprecipitation or “disease”? *Econ. Geol.* 86, 1070–1082.
- Bourdon, E., Eissen, J.P., Monzier, M., Robin, C., Martin, H., Cotton, J., Hall, M., 2002. Adakite-like Lavas from Antisana Volcano (Ecuador): Evidence for slab melt Metasomatism beneath the Andean North Volcanic Zone. *J. Petrol.* 43, 199–217.
- Briqueu, L., Jayoy, M., Lancelot, J.R., Tatsumoto, M., 1986. Isotope geochemistry of recent magmatism in the Aegean arc: Sr, Nd, Hf, and O isotopic ratios in the lavas of Milos and Santorini-geodynamic implication. *Earth Planet. Sci. Lett.* 80, 41–54.
- Brown, M., 2010. Melting of the continental crust during orogenesis: the thermal, rheological and compositional consequences of melt transport from lower to upper continental crust. *Can. J. Earth Sci.* 47, 655–694.
- Castro, A., Aghazadeh, M., Badrzadeh, Z., Chichorro, M., 2013. Late Eocene-Oligocene post-collisional monzonitic intrusions from the Alborz magmatic belt, NW Iran. An example of monzonite magma generation from a metasomatized mantle source. *Lithos* 180–181, 109–127.
- Chung, S.L., Liu, D.Y., Ji, J.Q., Chu, M.F., Lee, H.Y., Wen, D.J., Lo, C.H., Lee, T.Y., Qian, Q., Zhang, Q., 2003. Adakites from continental collision zones: melting of thickened

- lower crust beneath southern Tibet. *Geology* 31, 1021–1024.
- Condie, K.C., 1989. Geochemical changes in basalts and andesites across the Archean-Proterozoic boundary: identification and significance. *Lithos* 23, 1–18.
- Cox, K.G., Bell, J.D., Pankhurst, R.J., 1979. The Interpretation of Igneous Rocks. Allen and Unwin, London, pp. 450.
- Defant, M.J., Drummond, M.S., 1990. Derivation of some modern arc magmas by melting of young subducted lithosphere. *Nature* 347, 662–665.
- Defant, M.J., Kepezhinskas, P., Defant, M.J., Xu, J.F., Kepezhinskas, P., Wang, Q., Zhang, Q., Xiao, L., 2002. Adakites: some variations on a theme. *Acta Petrol. Sin.* 18, 129–142.
- Delavari, M., Amini, S., Schmitt, A.K., McKeegan, K.D., Harrison, T.M., 2014. U-Pb geochronology and geochemistry of Bibi-Maryam pluton, eastern Iran: implication for the late stage of the tectonic evolution of the Sistan Ocean. *Lithos* 200–201, 197–211.
- Dilek, Y., Altunkaynak, A., 2007. Cenozoic crustal evolution and mantle dynamics of post-collisional magmatism in Western Anatolia. *Inter. Geol. Rev.* 49, 431–453.
- Doe, B.R., Zartman, R.E., 1979. Plumbotectonics I, the Phanerozoic, In: Barnes, H.L. (Ed.), *Geochemistry of Hydrothermal Ore Deposits*, 2nd ed. John Wiley and Sons, New York, pp. 22–70.
- Ducea, M., Saleeby, J., 1998. Crustal recycling beneath continental arcs: silica-rich glass inclusions in ultramafic xenoliths from the Sierra Nevada, California. *Earth Planet. Sci. Lett.* 156, 101–116.
- Fitton, J.G., James, D., Kempton, P.D., Ormerod, D.S., Leeman, W.P., 1988. The role of lithospheric mantle in the generation of Late Cenozoic basic magmas in the Western United States. *J. Petrol.* 1, 331–349.
- Foley, S.F., Tiepolo, M., Vannucci, R., 2002. Growth of early continental crust controlled by melting of amphibolite in subduction zones. *Nature* 417, 637–640.
- Foley, S.F., Wheller, G.E., 1990. Parallels in the origin of the geochemical signatures of island arc volcanoes and continental potassiac igneous rocks: the role of residual titanates. *Chem. Geol.* 85, 1–18.
- Frey, F.A., Chappell, B.W., Roy, S.D., 1978. Fractionation of rare-earth elements in the Tuolumne Intrusive Series, Sierra Nevada batholith, California. *Geology* 6, 239–242.
- Fu, L., Wei, J., Husky, T.M., Chen, H., Tan, J., Li, Y., Shi, W., Chen, C., Zhao, S., 2012. The Cretaceous Duimiangou adakite-like intrusion from the Chifeng region, northern North China Craton: crustal contamination of basaltic magma in an intracontinental extensional environment. *Lithos* 134–135, 273–288.
- Gao, S., Rudnick, R.L., Yuan, H.L., Liu, X.M., Liu, Y.S., Xu, W.L., Lin, W.L., Ayers, J., Wang, X.C., Wang, Q.H., 2004. Recycling lower continental crust in the North China craton. *Nature* 432, 892–897.
- Gao, Y., Hou, Z., Kamber, B.S., Wei, R., Meng, X., Zhao, R., 2007. Adakite-like porphyries from the southern Tibetan continental collision zones: evidence for slab melt metasomatism. *Contrib. Miner. Petrol.* 153, 105–120.
- Ge, X., Li, X., Chen, Z., Li, W., 2002. Geochemistry and petrogenesis of Jurassic high Sr/low Y granitoids in eastern China: constraints on crustal thickness. *Chin. Sci. Bull.* 47, 11.
- Ghasemi Siani, M., Mehrabi, B., Azizi, H., Wilkinson, C.M., Ganerod, M., 2015. Geochemistry and geochronology of the volcano-plutonic rocks associated with the Goljeh epithermal gold mineralization, NW Iran. *Open Geosci.* 7, 207–222.
- Ghasemi, A., Talbot, C.J., 2006. A new tectonic scenario from the Sanandaj-Sirjan Zone (Iran). *J. Asian Earth Sci.* 26, 683–693.
- Gorton, M.P., Schandl, E.S., 2000. From continents to island arcs: a geochemical index of tectonic setting for arc related and within-plate felsic or intermediate volcanic rocks. *Can. Mineral.* 38, 1065–1073.
- Green, T.H., 1994. Experimental studies of trace element partitioning applicable to igneous petrogenesis Sedona 16 years later. *Chem. Geol.* 117, 1–36.
- Green, T.H., 1980. Island arc and continent-building magmatism: a review of petrogenetic models based on experimental petrology and geochemistry. *Tectonophysics* 63, 367–385.
- Gromet, L.P., Silver, L.T., 1987. REE variations across the Peninsular Ranges Batholith: implications for batholithic petrogenesis and crustal growth in magmatic arcs. *J. Petrol.* 28, 75–125.
- Gust, D.A., Arculus, R.A., Kersting, A.B., 1997. Aspects of magma sources and processes in the Honshu arc. *Can. Mineral.* 35, 347–365.
- Hanson, G.N., 1980. Rare earth elements in petrogenetic studies of igneous systems. *Ann. Rev. Earth Planet. Sci.* 8, 371–406.
- Harris, N.B.W., Pearce, J.A., Tindle, A.G., 1986. Geochemical characteristics of collision-zone magmatism. In: Coward, M.P., Ries, A.C. (Eds.), *Collision Tectonics*. Geological Society of London, Special Publication, 19, 67–81.
- Haschke, M., Ahmadian, J., Murata, M., McDonald, I., 2010. Copper mineralization prevented by arc-root delamination during Alpine-Himalayan collision central Iran. *Econ. Geol.* 105, 855–865.
- Hatzfeld, D., Molnar, P., 2010. Comparisons of the kinematics and deep structures of the Zagros and Himalaya and of the Iranian and Tibetan Plateaus, and geodynamic implications. *Rev. Geophys.* 48, RG2005.
- Hedenquist, J.W., Arribas, A., Gonzalez-Urén, E., 2000. Exploration for epithermal gold deposits. *Rev. Econ. Geol.* 13, 245–277.
- Hedenquist, J.W., Arribas, A., 1998. Evolution of an intrusion-centered hydrothermal system: far southeast Lepanto porphyry and epithermal Cu-Au deposits, Philippines. *Econ. Geol.* 93 (4), 373–404.
- Hirayama, K., Samimi, M., Zahedi, M., Hushmandzadeh, A., 1966. Geology of Tarom district, western part (Zanjan area, North West Iran). *G.S. I. Rep.* No. 8 31.
- Hofmann, A.W., Jochum, K.P., Seufert, M., White, W.M., 1986. Nb and Pb in oceanic basalts: new constraints on mantle evolution. *Earth Planet. Sci. Lett.* 79, 33–45.
- Hosseinzadeh, M.R., Maghfouri, S., Moayyed, M., 2014. Petrology, geochemistry and alteration at the polymetallic (Cu-Pb-Zn) vein and veinlet mineralization in the Lubin-Zardeh area, north east Zanjan. *Sci. Quat. J. Geosci.* 24 (99), 41–52 (in Persian with English abstract).
- Hou, Z.Q., Gao, Y.F., Qu, X.M., Rui, Z.Y., Mo, X.X., 2004. Origin of adakitic intrusives generated during midMiocene east–west extension in southern Tibet. *Earth Planet. Sci. Lett.* 220, 139–155.
- Huang, W.L., Wyllie, P.J., 1986. Phase relationships of gabbro-tonalite-granite H2O at 15 kbar with applications to differentiation and anatexis. *Am. Mineral.* 71, 301–316.
- Jahangiri, H., 2007. Post-collisional Miocene adakitic volcanism in NW Iran: geochemical and geodynamic implications. *J. Asian Earth Sci.* 30, 433–447.
- Jahn, B.M., Zhang, J.Q., 1984. Archean granulite gneisses from eastern Sino-Korean Province, China: rare earth geochemistry and tectonic implication. *Contrib. Miner. Petro.* 85, 224–243.
- Jamali, H., Mehrabi, B., 2015. Relationships between arc maturity and Cu–Mo–Au porphyry and related epithermal mineralization at the Cenozoic Arasbaran magmatic belt. *Ore Geol. Rev.* 65, 481–501.
- Jull, M., Kelemen, P.B., 2001. On the conditions for lower crustal convective instability. *J. Geophys. Res.* 106, 6423–6446.
- Kananian, A., Sarjoughian, F., Nadimi, A.R., Ahmadian, J., Ling, W., 2014. Geochemical characteristics of the Kuh-e Dom intrusion, Urumieh-Dokhtar Magmatic Arc (Iran): implications for source regions and magmatic evolution. *J. Asian Earth Sci.* 90, 137–148.
- Karsli, O., Dokur, A., Uysal, I., Ketenci, M., Chen, B., Kandemir, R., 2012. Deciphering the shoshonitic monzonites with I-type characteristic, the Sısdagli pluton, NE Turkey: magmatic response to continental lithospheric thinning. *J. Asian Earth Sci.* 51, 45–62.
- Kay, R.W., Kay, S.M., 1991. Creation and destruction of lower continental crust. *Geol. Rund.* 80, 259–278.
- Kay, R.W., Kay, S.M., 1993. Delamination and delamination magmatism. *Tectonophysics* 219, 177–189.
- Kay, S.M., Ramos, V.A., Marquez, M., 1993. Evidence in Cerro Pampa volcanic rocks of slab melting prior to ridge trench collision in southern South America. *J. Geol.* 101, 703–714.
- Kepezhinskas, P.K., Defant, M.J., Drummond, M.S., 1995. Na metasomatism in the island-arc mantle by slab melt-peridotite interaction: evidence from mantle interaction: Evidence from mantle xenoliths in the north Kamchatka arc. *J. Petrol.* 36, 1505–1527.
- Kerrick, R., Wyman, D.A., 1997. Review of developments in trace-element fingerprinting of geodynamic settings and their implications for mineral exploration. *Aust. J. Earth Sci.* 44, 465–487.
- Kesson, S.E., Ringwood, A.E., 1989. Slab-mantle interactions, Sheared and refertilized garnet peridotite xenolith samples of Wadati-Benioff Zones? *Chem. Geol.* 78, 83–96.
- Kouhestani, H., Mokhtari, M.A.A., Chang, Z., Johnson, C.A., 2018. Intermediate sulfidation type base metal mineralization at Aliabad-Khanchy, Tarom-Hashtjin metallogenic belt, NW Iran. *Ore Geol. Rev.* 93, 1–18.
- Kouhestani, H., Mokhtari, M.A.A., Qin, K.Z., Zhao, J.X., 2019. Fluid inclusion and stable isotope constraints on ore genesis of the Zajkan epithermal base metal deposit, Tarom-Hashtjin metallogenic belt, NW Iran. *Ore Geol. Rev.* 109, 564–584.
- Lai, S.C., Liu, C.Y., Yi, H.S., 2003. Geochemistry and petrogenesis of Cenozoic Andesite-Dacite associations from the Hoh Xil Region, Tibetan Plateau. *Inter. Geol. Rev.* 45, 998–1019.
- Li, J.X., Qin, K.Z., Li, G.M., Evans, N.J., Zhao, J.X., Cao, M.J., Fang, H., 2016. The Nadun Cu–Au mineralization, central Tibet: root of a high sulfidation epithermal deposit. *Ore Geol. Rev.* 78, 371–387.
- Li, S.N., Ni, P., Bao, T., Li, C.Z., Xiang, H.L., Wang, G.G., Huang, B., Chi, Z., Dai, B.Z., Ding, J.Y., 2018. Geology, fluid inclusion, and stable isotope systematics of the Dongyang epithermal gold deposit, Fujian Province, southeast China: Implications for ore genesis and mineral exploration. *J. Geochem. Expl.* 195, 16–30.
- Liegeois, J.P., Navez, J., Hertogen, J., Black, R., 1998. Contrasting origin of post-collisional high-K calc-alkaline and shoshonitic versus alkaline and peralkaline granitoids. The use of sliding normalization. *Lithos* 45, 1–28.
- Liu, S.A., Li, S., He, Y., Huang, F., 2010. Geochemical contrasts between early Cretaceous ore-bearing and ore barren high-Mg adakites in central-eastern China: implications for petrogenesis and Cu–Au mineralization. *Geochim. Cosmochim. Acta* 74, 7160–7178.
- Mahoney, J.J., Frei, R., Tejada, M.L.G., Mo, X.X., Leat, P.T., Nagler, T.P., 1998. Tracing the Indian Ocean mantle domain through time: isotopic results from old west Indian, east Tethyan, and South Pacific seafloor. *J. Petrol.* 39, 1285–1306.
- Maniar, P.D., Piccoli, P.M., 1989. Tectonic discrimination of granitoids. *Geol. Soc. Am. Bull.* 101, 635–643.
- Martin, H., 1999. The adakitic magmas: modern analogues of Archean granitoids. *Lithos* 46, 411–429.
- Mehrabi, B., Ghasemi Siani, M., Goldfarb, R., Azizi, H., Ganerod, M., Marsh, E.E., 2016. Mineral assemblages, fluid evolution and genesis of polymetallic epithermal veins, Gulojeh district, NW Iran. *Ore Geol. Rev.* 78, 41–57.
- Mirnejad, H., Lalonde, A.E., Obeid, M., Hassanzadeh, J., 2013. Geochemistry and petrogenesis of Mashhad granitoids: An insight into the geodynamic history of the Paleo-Tethys in northeast of Iran. *Lithos* 170–171, 105–116.
- Mo, X., Hou, Z., Niu, Y., Dong, G., Qu, X., Zhao, Z., Yang, Z., 2007. Mantle contributions to crustal thickening during continental collision: Evidence from Cenozoic igneous rocks in southern Tibet. *Lithos* 96, 225–242.
- Moayyed, M., 2001. Investigation of Tertiary Volcano-plutonic Bodies in West Alborz-Azerbaijan (Hashtjin area): Ph.D. thesis. University of Shahid Beheshti, Tehran, Iran, pp. 296 p. (in Persian with English abstract).
- Muir, R.J., Weaver, S.D., Bradshaw, J.D., Eby, G.N., Evans, J.A., 1995. Geochemistry of the Cretaceous Separation Point Batholith, New Zealand: granitoid magmas formed by melting of mafic lithosphere. *J. Geol. Soc. London* 152, 689–701.
- Müller, D., Groves, D.I., 1993. Direct and indirect associations between potassiac igneous rocks, shoshonites and gold-copper deposits. *Ore Geol. Rev.* 8, 383–406.
- Müller, D., Groves, D.I., 1997. Potassiac Igneous Rocks and Associated Gold-Copper

- Mineralization, 3rd ed. Springer-Verlag, Berlin, pp. 238p.
- Müller, D., Groves, D.I., 2000. Potassic Igneous Rocks and Associated Gold–copper Mineralization 252.
- Muntean, J.L., Einaudi, M.T., 2001. Porphyry-epithermal transition: Maricunga Belt, Northern Chile. *Econ. Geol.* 96, 743–772.
- Nabatian, G., Ghaderi, M., Neubauer, F., Honarmand, M., Xiaoming, L., Dong, Y., Jiang, S.H., Quadt, A., Bernroder, M., 2014. Petrogenesis of Tarom high-potassic granitoids in the Alborz-Azerbaijan belt, Iran: geochemical, U-Pb zircon and Sr-Nd-Pb isotopic constraints. *Lithos* 184–187, 324–345.
- Nabatian, G., Jiang, S.Y., Honarmand, M., Neubauer, F., 2016. Zircon U-Pb ages, geochemical and Sr–Nd–Pb–Hf isotopic constraints on petrogenesis of the Tarom-Olya pluton, Alborz magmatic belt, NW Iran. *Lithos* 244, 43–58.
- Omrami, J., Agard, P., Whitechurch, H., Benoit, M., Prouteau, G., Jolivet, L., 2008. Arc-magmatism and subduction history beneath the Zagros Mountains, Iran: a new report of adakites and geodynamic consequences. *Lithos* 106, 380–398.
- Oyarzun, R., Marquez, A., Lillo, J., Lopez, I., Rivera, S., 2001. Giant versus small porphyry copper deposits of Cenozoic age in northern Chile: adakitic versus normal calcalkaline magmatism. *Miner. Deposita* 36, 794–798.
- Pearce, J.A., 1982. Trace element characteristics of lavas from destructive plate boundaries. In: Thorpe, R.S. (Ed.), Andesites. Wiley, New York, pp. 525–548.
- Pearce, J.A., 1983. Role of the sub-continental lithosphere in magma genesis at active continental margins. In: Hawkesworth, C.J., Norry, M.J. (Eds.), Continental Basalts and Mantle Xenoliths. Shiva, Nantwich, pp. 230–249.
- Pearce, J.A., Harris, N.B.W., Tindle, A.G., 1984. Trace element discrimination diagrams for the tectonic interpretation of granitic rocks. *J. Petrol.* 25, 956–983.
- Pearce, J.A., Norry, M.J., 1979. Petrogenetic implications of Ti, Zr, Y, and Nb variations in volcanic rocks. *Contrib. Miner. Petrol.* 69, 33–47.
- Peccerillo, A., Taylor, S.R., 1976. Geochemistry of Eocene calc-alkaline volcanic rocks from the Kastamonu area, Northern Turkey. *Contrib. Miner. Petrol.* 58, 63–81.
- Petford, N., Atherton, M., 1996. Na-rich Partial melts from newly underplated basaltic crust: the Cordillera Blanca Batholith, Peru. *J. Petrol.* 37, 1491–1521.
- Pudack, C., Halter, W.E., Heinrich, C.A., Pettke, T., 2009. Evolution of magmatic vapor to gold-rich epithermal liquid: the porphyry to epithermal transition at Nevados de Famatina, Northwest Argentina. *Econ. Geol.* 104, 449–477.
- Qu, X.M., Hou, Z.Q., Li, Y.G., 2004. Melt components derived from a subducted slab in late orogenic ore-bearing porphyries in the Gangdese copper belt, southern Tibetan plateau. *Lithos* 74, 131–148.
- Rahmani, S., 2010. Prospecting, Exploration and Geological Mapping (1: 25,000) of Lubin – Zardeh gold exploration area (Taram Zone), (in Persian) Geological and Mineral Exploration Survey of Iran, p. 283.
- Rahmani, S., Zamanian, H., Zareisahamieh, R., 2018. Geochemical characteristics of igneous host rocks associated of Lubin-Zardeh epithermal gold and base metal deposit, NW of Iran. *Iran. Geosci. J* Accepted manuscript (in Persian with English abstract).
- Rapp, R.P., Shimizu, N., Norman, M.D., Applegate, G.S., 1999. Reaction between slab-derived melts and peridotite in the mantle wedge: experimental constraints at 38 GPa. *Chem. Geol.* 160, 335–356.
- Rapp, R.P., Shimizu, N., Norman, M.D., 2003. Growth of early continental crust by partial melting of eclogite. *Nature* 425, 605–609.
- Rapp, R.P., Watson, E.B., 1995. Dehydration melting of metabasalt at 8–32 kbar: Implications for continental growth and crust-mantle recycling. *J. Petrol.* 36, 891–931.
- Rapp, R.P., Watson, E.B., Miller, C.F., 1991. Partial melting of amphibolite/eclogite and the origin of Archean trondhjemites and tonalities. *Precambr. Res.* 51, 1–25.
- Rapp, R.P., Xiao, L., Shimizu, N., 2002. Experimental constraints on the origin of potassium-rich adakite in east China. *Acta Petrol. Sin.* 18, 293–311.
- Rezaei-Kahkhaei, M., Galindo, C., Pankhurst, R.J., Esmaeily, D., 2011. Magmatic differentiation in the calc-alkaline Khalkhab-Neshveh pluton, Central Iran. *J. Asian Earth Sci.* 42, 499–514.
- Richards, J.P., 2009. Post subduction porphyry Cu–Au and epithermal Au deposits: products of remelting of subduction-modified lithosphere. *Geology* 37, 247–250.
- Richards, J.P., Spell, T., Rameh, E., Razique, A., Fletcher, T., 2012. High Sr/Y magmas reflect arc maturity, high magmatic water content, and porphyry Cu ± Mo ± Au potential: examples from the Tethyan Arcs of Central and Eastern Iran and Western Pakistan. *Econ. Geol.* 107, 295–332.
- Rollinson, H., 1993. Using Geochemical Data: Evaluation, Presentation, Interpretation. Longman Scientific and Technical, London, pp. 266–315.
- Rudnick, R.L., Fountain, D.M., 1995. Nature and composition of the continental crust: a lower crustal perspective. *Rev. Geophys.* 33, 267–309.
- Sabeva, R., Mladenova, V., Mogessie, A., 2017. Ore petrology, hydrothermal alteration, fluid inclusions, and sulfur stable isotopes of the Milin Kamak intermediate sulfidation epithermal Au-Ag deposit in Western Srednogorie, Bulgaria. *Ore Geol. Rev.* <https://doi.org/10.1016/j.oregeorev>.
- Sack, R.O., Carmichael, I.S.E., Rivers, M., Chiorso, M.S., 1980. Ferric-ferrous equilibria in natural silicates liquids at 1 bar. *Contrib. Miner. Petrol.* 75, 369–376.
- Sarjoughian, F., Kananian, A., Haschke, M., Ahmadian, J., Ling, W., Zong, K., 2012. Magma mingling and hybridization in the Kuh-e Dom pluton, Central Iran. *J. Asian Earth Sci.* 54–55, 49–63.
- Sen, C., Dunn, T., 1994. Dehydration melting of a basaltic composition amphibolite at 1.5 and 2.0 GPa: implications for the origin of adakites. *Contrib. Miner. Petrol.* 117, 394–409.
- Shafiei, B., Haschke, M., Shahabpour, J., 2009. Recycling of orogenic arc crust triggers porphyry Cu mineralization in Kerman Cenozoic arc rocks, southeastern Iran. *Miner. Deposita* 44, 265–283.
- Shellnutt, J.G., Lee, T.Y., Brookfield, M.E., Chung, S.L., 2014. Correlation between magmatism of the Ladakh Batholith and plate convergence rates during the India-Eurasia collision. *Gondwana Res.* 26, 1051–1059.
- Shomali, Z.H., Keshvari, F., Hassanzadeh, J., Mirzaei, N., 2011. Lithospheric structure beneath the Zagros collision zone resolved by non-linear teleseismic tomography. *Geophys. J. Inter.* 187, 394–406.
- Sisson, T.W., 1994. Hornblende-melt trace-element partitioning measured by ion microprobe. *Chem. Geol.* 117, 331–334.
- Skjerlie, K.P., Patiño Douce, A.E., 2002. The fluid-absent partial melting of a zoisite-bearing quartz eclogite from 1.0 to 3.2 GPa: implications for melting in thickened continental crust and for subduction-zone processes. *J. Petrol.* 43, 291–314.
- Sodoudi, F., Yuan, X., Kind, R., Heit, B., Sadikhouy, A., 2009. Evidence for a missing crustal root and a thin lithosphere beneath the Central Alborz by receiver function studies. *Geophys. J. Int.* 177, 733–742.
- Springer, W., Seck, H.A., 1997. Partial fusion of basic granulites at 5 to 15 kbar: Implications for the origin of TTG magmas. *Contrib. Miner. Petrol.* 127, 30–45.
- Stacey, J.S., Kramers, J.D., 1975. Approximation of terrestrial lead isotope evolution by a two stage model. *Earth Planet. Sci. Lett.* 26, 207–221.
- Stöcklin, J., 1968. Structural history and tectonics of Iran, a review. *Am. Assoc. Pet. Geol. Bull.* 52, 1229–1258.
- Stöcklin, J., 1971. Stratigraphic lexicon of Iran; Part 1. Geological Survey of Iran, Tehran.
- Sun, S.S., McDonough, W.F., 1989. Chemical and isotopic systematics of oceanic basalts; implications for mantle composition and processes, in: Saunders A.D., Norry, M.J., (Eds.), *Magmatism in the ocean basins*, Geology Society London 42, 313–345.
- Tatsumi, Y., 1986. Chemical characteristics of fluid phase released from a subduction lithosphere and origin of arc magma: evidence from high-pressure experiments and natural rocks. *J. Volcanol. Geoth. Res.* 29, 293–309.
- Thieblemont, D., Stein, G., Lescuyer, J.L., 1997. Gisements épithermaux et porphyriques: La connexion adakite. Académie de Sciences Paris, Comptes Rendus 325, 103–109.
- Tribuzio, R., Thirlwall, M.F., Vannucci, R., Matthew, F., 2004. Origin of the gabbro-peridotite association from the Northern Apennine Ophiolites (Italy). *J. Petrol.* 45, 1109–1124.
- Verdel, C., Wernicke, B.P., Hassanzadeh, J., Guest, B., 2011. A Paleogene extensional arc flare-up in Iran. *Tectonics* 30, TC3008. <http://dx.doi.org/10.1029/2010TC002809>.
- Waight, T.E., Weaver, S.D., Muir, R.J., 1998. The Hohonu Batholith of North Westland, New Zealand: granitoid compositions controlled by source H2O contents and generated during tectonic transition. *Contrib. Mineral. Petrol.*, 225–239.
- Wang, Q., Wyman, D.A., Xu, J.F., Zhao, Z.H., Jian, P., Xiong, X.L., Bao, Z.W., Li, C.F., Bai, Z.H., 2006a. Petrogenesis of Cretaceous adakitic and shoshonitic igneous rocks in the Luzong area, Anhui Province (eastern China): implications for geodynamics and Cu–Au mineralization. *Lithos* 89, 424–446.
- Wang, Q., Xu, J.F., Jian, P., Bao, Z.W., Zhao, Z.H., Li, C.F., Xiong, X.L., Ma, J.L., 2006b. Petrogenesis of Adakitic porphyries in an extensional tectonic setting, Dexing, South China: implications for the genesis of porphyry copper mineralization. *J. Petrol.* 47, 119–144.
- Wang, Q., Wyman, D.A., Xu, J., Jian, P., Zhao, Z., Li, C., Xu, W., Ma, J., He, B., 2007. Early Cretaceous adakitic granites in the northern Dabie Complex, central China: implications for partial melting and delamination of thickened lower crust. *Geochim. Cosmochim. Acta* 71, 2609–2636.
- Wang, Q., Xu, J.F., Zhao, Z.H., Bao, Z.W., Xu, W., Xiong, X.L., 2004a. Cretaceous high-potassium intrusive rocks in the Yueshan-Hongzhen area of east China: adakites in an extensional tectonic regime within a continent. *Geochim. J.* 38, 417–434.
- Wang, Q., Zhao, Z.H., Bao, Z.W., Xu, J.F., Liu, W., Li, C.F., Bai, Z.H., Xiong, X.L., 2004b. Geochimistry and petrogenesis of the Tongshankou and Yinzu adakitic intrusive rocks and the associated porphyry copper-molybdenum mineralization in southeast Hubei, east China. *Resour. Geol.* 54, 137–152.
- Weaver, B.L., Tarney, J., 1984. Estimating the composition of the continental crust: an empirical approach. *Nature* 310, 575–577.
- Wedepohl, K.H., 1995. The composition of the continental crust. *Geochim. Cosmochim. Acta* 59, 1217–1232.
- Whitney, D.L., Evans, B.W., 2010. Abbreviations for names of rock-forming minerals. *Am. Mineral.* 95, 185–187.
- Wiggins, L.B., Craig, J.R., 1980. Reconnaissance of the Cu–Fe–Zn–S system: Sphalerite phase relations. *Econ. Geol.* 75, 742–751.
- Wilson, M., 1989. Igneous Petrogenesis: A Global Tectonic Approach. Harper Collins Academic.
- Winther, K.T., 1996. An experimentally based model for the origin of tonalitic and trondhjemite melts. *Chem. Geol.* 127, 43–59.
- Wolf, M.B., Wyllie, P.J., 1994. Dehydration-melting of amphibolite at 10 kbar: the effects of temperature and time. *Contrib. Miner. Petrol.* 115, 369–383.
- Woodhead, J., Egging, S., Gamble, J., 1993. High field strength and transition element systematics in island arc and back-arc basin basalts: evidence for multi-phase melt extraction and a depleted mantle wedge. *Earth Planet. Sci. Lett.* 114, 491–504.
- Xu, J.F., Castillo, P.R., 2004. Geochemical and Nd–Pb isotopic characteristics of the Tethyan asthenosphere: implications for the origin of the Indian Ocean mantle domain. *Tectonophysics* 393, 9–27.
- Xu, J.F., Castillo, P.R., Chen, F.R., Niu, H.C., Yu, X.Y., Zhen, Z.P., 2003. Geochemistry of late Paleozoic mafic igneous rocks from the Kuerti area, Xinjiang, northwest China: implications for backarc mantle evolution. *Chem. Geol.* 193, 137–154.
- Xu, J.F., Shinjio, R., Defant, M.J., Wang, Q., Rapp, R.P., 2002. Origin of Mesozoic adakitic intrusive rocks in the Ningzhen area of east China: partial melting of delaminated lower continental crust? *Geology* 30, 1111–1114.
- Yang, Z.M., Hou, Whit, Z.Q., Chang, N.C., Song, Z.Q., Li, Y.C., 2009. Geology of the post-collisional porphyry copper-molybdenum deposit at Qulong, Tibet. *Ore Geol. Rev.* 36, 133–159.
- Yardley, B.W.D., Valley, J.W., 1997. The petrologic case for a dry lower crust. *J. Geophys. Res.* 102, 12173–12185.
- Yasami, N., Ghaderi, M., 2019. Distribution of alteration, mineralization and fluid inclusion features in porphyry-high sulfidation epithermal systems: the Chodarchay

- example, NW Iran. *Ore Geol. Rev.* 104, 227–245.
- Yasami, N., Ghaderi, M., Alfonso, P., 2018. Sulfur isotope geochemistry of the Chodarchay Cu-Au deposit, Tarom, NW Iran. *N. Jb. Miner. Abh. (J. Min. Geochem.)* 195 (2), 101–113.
- Yasami, N., Ghaderi, M., Madanipour, S., Taghilou, B., 2017. Structural control on overprinting high-sulfidation epithermal on porphyry mineralization in the Chodarchay deposit, northwestern Iran. *Ore Geol. Rev.* 86, 212–224.
- Yogodzinski, G.M., Kay, R.W., Volynets, O.N., Koloskov, A.V., Kay, S.M., 1995. Magnesian andesite in the western Aleutian Komandorsky region: implications for slab melting and processes in the mantle wedge. *Geol. Soc. Am. Bull.* 107, 505–519.
- Zamanian, H., Rahmani, S., Zareisahamieh, R., 2019. Fluid inclusion and stable isotope study of the Lubin-Zardeh epithermal Cu-Au deposit in Zanjan Province, NW Iran: Implications for ore genesis. *Ore Geol. Rev.* 112, 103014. <https://doi.org/10.1016/j.oregeorev.2019.103014>. (accepted manuscript).
- Zamanian, H., Rahmani, S., Zareisahamieh, R., Borna, B., 2016. Ore genesis study of the Cu-Au vein type deposit in the Tarom granitoid in Lohne districts, Zanjan province, Iran. *Iran. Geosci. J.* 98, 255–282 (in Persian with English abstract).
- Zarasvandi, A., Liaghat, S., Zentilli, M., 2005. Geology of the Darreh-Zereshk and Ali-Abad Porphyry Copper Deposits, Central Iran. 47, 620–646.
- Zarasvandi, A., Liaghat, S., Zentilli, M., Reynolds, P.H., 2007. $^{40}\text{Ar}/^{39}\text{Ar}$ geochronology of alteration and petrogenesis of porphyry copper-related granitoids in the Darreh-Zereshk and Ali-Abad area, central Iran. *Explor. Min. Geol.* 16, 11–24.
- Zarasvandi, A., Rezaei, M., David, L., Pourkaseb, H., 2015. Geochemistry and Fluid characteristics of the Dalli porphyry Cu-Au Deposit, Central Iran. *J. Asian Earth Sci Accepted Manuscript*.
- Zen, E.An., 1986. Alluminum enrichment in silicate melts by fractional crystallization: some mineralogical and petrographic constraints. *Journal of Petrology* 27, 1095–1118.
- Zhang, Q., Wang, Y., Liu, W., Wang, Y.L., 2002. Adakite: its characteristics and implications (in Chinese). *Geol. Bull. China* 2, 431–435.
- Zhang, Q., Wang, Y., Qian, Q., 2001. The characteristics and tectonic–metallogenic significances of the Mesozoic adakitic rocks in eastern China (in Chinese). *Acta Petrol. Sin.* 17, 236–244.
- Zhao, J.H., Zhou, M.F., 2008. Neoproterozoic adakitic plutons in the northern margin of the Yangtze Block, China: partial melting of a thickened lower crust and implications for secular crustal evolution. *Lithos* 104, 231–248.
- Zhou, M.F., Yan, D.P., Wang, C.L., Qi, L., Kennedy, A., 2006. Subduction-related origin of the 750 Ma Xuelongbao adakitic complex (Sichuan Province, China): implications for the tectonic setting of the giant Neoproterozoic magmatic event in South China. *Earth Planet. Sci. Lett.* 248, 286–300.
- Zindler, A., Hart, S.R., 1986. Chemical geodynamics. *Annu. Rev. Earth Planet. Sci.* 14, 493–571.